CHARACTERISTIC X-RAY, PHOTOELECTRON AND COMPTON-SCATTERED PHOTON ESCAPE FROM A HPGe DETECTOR

A THESIS SUBMITTED TO
THE GRADUATE SCHOOL OF NATURAL AND APPLIED SCIENCES
OF
THE MIDDLE EAST TECHNICAL UNIVERSITY

BY

ERCAN YILMAZ

IN PARTIAL FULFILLMENT OF THE REQUIREMENTS FOR THE DEGREE OF

DOCTOR OF PHILOSOPHY

IN

THE DEPARTMENT OF PHYSICS

APRIL 2003

ABSTRACT

CHARACTERISTIC X-RAY, PHOTOELECTRON AND COMPTON-SCATTERED PHOTON ESCAPE FROM A HPGe DETECTOR

Yılmaz, Ercan
Ph.D., Department of Physics

Supervisor: Assoc. Prof. Dr. Cüneyt Can

April 2003, 64 pages.

Escape of photoelectrons, Compton-scattered photons and Ge X-rays from a HPGe detector was studied as a function of energy in the range 8-52 keV. A variable-energy source producing Cu, Rb, Mo, Ag, Ba, and Tb X-rays was used. All three mechanisms for energy loss were observed in the same experiment for Ba and Tb, while only X-ray and photoelectron escapes were evident in the spectra for Ag, Mo, Rb, and Cu. Spectral features and possible mechanisms for partial energy deposition were investigated. A Monte Carlo program was used to simulate the relevant interactions and to estimate the escape probabilities.

Keywords: X-Ray escape, Photoelectron and Compton escape, HPGe detector, Monte Carlo.

ÖZ

HPGe DEDEKTÖRDE KARAKTERİSTİK X-IŞINI, FOTOELEKTRON VE COMPTON SAÇILMASI KAÇAĞI

Yılmaz, Ercan
Ph.D., Fizik Bölümü

Danışman: Doç. Dr. Cüneyt Can

Nisan 2003, 64 sayfa.

Bir HPGe dedektöründen fotoelektron, Compton saçılımına uğrayan fotonlar ve Ge X-ışınları kaçakları 8-52 keV aralığında enerjinin bir fonksiyonu olarak incelendi. Cu, Rb, Mo, Ag, Ba, ve Tb X-ışınları oluşturan, değiştirilebilir enerjili bir kaynak kullanıldı. Ba ve Tb için, enerji kaybı mekanizmalarının üçü de aynı deneyde gözlenirken, Ag, Mo, Rb ve Cu için spektrumlarda sadece X-ışını ve fotoelektron kaçakları görüldü. Spektral özellikler ve kısmi enerji depolanması için olası mekanizmalar araştırıldı. Etkileşmelerin simülasyonunu yapmak ve kaçış olasılıklarını tahmin etmek için bir Monte Carlo programı kullanıldı.

Anahtar sözcükler: X-ışını kaçağı, fotoelektron ve Compton kaçağı, HPGe dedektörü, Monte Carlo.

ACKNOWLEDGEMENT

I would like to express my gratitude to all those who gave me the opportunity to complete this thesis. I want to thank the Department of Physics for giving me permission to commence this thesis in the first instance, to do the necessary research work and to use departmental instruments. I have, furthermore, to thank all the secretaries of Dean's Office for their kind help.

I am deeply indebted to my supervisor Assoc. Prof. Dr. Cüneyt Can whose help, stimulating suggestions and encouragement helped me throughout my research and writing of this thesis.

My former supervisor, Prof. Dr. Bülent G. Akınoğlu of the Department of Physics supported me in my research work. I want to thank him for all his help, support, interest and valuable hints. Especially, I am obligated to thank my roommate, Cem Yüce, for his patience.

I would like to thank Ankara Nuclear Research and Training Center and the Department of Mechanical Engineering (METU) for allowing me to use their apparatus for my research.

Especially, I would like to give my special thanks to my wife whose patient love enabled me to complete this work.

TABLE OF CONTENTS

CHAPTER

APPENDICES

LIST OF TABLES

TABLES

LIST OF FIGURES

FIGURES

NOMENCLATURE

σ	Cross-section.
μ	Linear attenuation coefficient.
λ	Mean free path.
θ	Angle between the momentum vectors of the incident photon and the ejected photoelectron.
ω_i	Fluorescence yield.
r	Random number.
E_i	Initial photon energy; $E_i^{K_{\alpha 1}}$, $E_i^{K_{\alpha 2}}$, $E_i^{K_{\beta 1}}$, and $E_i^{K_{\beta 2}}$.
E_{pe}	Photoelectron energy; $E_{pe}^{K_{\alpha 1}}$, $E_{pe}^{K_{\alpha 2}}$, $E_{pe}^{K_{\beta 1}}$, and $E_{pe}^{K_{\beta 2}}$.
E_f	Compton-scattered photon energy; $E_f^{K_{\alpha 1}}$, $E_f^{K_{\alpha 2}}$, $E_f^{K_{\beta 1}}$, and $E_f^{K_{\beta 2}}$.
$E_{K\alpha}$	Germanium K_α X-ray energy.
$E_{K\beta}$	Germanium K_β X-ray energy.
E_{re}	Recoil electron energy; $E_{re}^{K_{\alpha 1}}$, $E_{re}^{K_{\alpha 2}}$, $E_{re}^{K_{\beta 1}}$, and $E_{re}^{K_{\beta 2}}$.
E_K^{ab}	K-shell absorption edge (K-shell binding energy).
E_L^{ab}	L-shell absorption edge (L-shell binding energy).
P_{Com}	Percentage Compton escape fractions.
P_{coh}	Percentage coherent escape fractions.
P_{pe}	Percentage photoelectron escape fractions.

$P_{X\alpha}$	Percentage K_α X-ray escape fractions.
$P_{X\beta}$	Percentage K_β X-ray escape fractions.

CHAPTER 1

INTRODUCTION

The inception of radiation detectors, particularly of semiconductor detectors, offered a wide range of applications in various fields of applied sciences. Along with these developments there has been a wide interest in determining line shapes, response functions and efficiency of these detectors. These efforts, ranging from experimental measurements to analytical calculations and from empirical fittings to Monte Carlo simulations have been so intense that determining the response function has been a "challenge" for scientists. Even though there seems to be as many response functions as there are detectors, some of the spectral features are common. However, it has been demonstrated by Papp and Campbell [1] that components of the response function, i.e. pulse-height distribution, could be different even when spectra obtained by several detectors of the same material are compared. Spectral features are based on physical mechanisms, which result in complete or partial deposition of energy. The major mechanisms involve interaction of primary radiation, i.e. X-rays or γ-rays, with the detector material, and interaction of characteristic X-rays, photoelectrons and Auger electrons in the detector. The role of electrons to and from electrical contact materials and dead layer of detectors has also been considered extensively.

The escape of characteristic X-rays produced in photo-absorption of primary photons has been studied in detail by many investigators. However, the role of photoelectrons, Auger electrons and Compton-scattered photons in partial deposition of energy has been under investigation only during the last decade. Furthermore, the importance of photoelectrons and Auger electrons has been studied mainly in the low-energy region and by using Si(Li) detectors.

Escape of Compton-scattered primary photons using an ^{241}Am source and a HPGe detector has been investigated only, to our knowledge, by Martin and Burns [2], and Pašić and Ilakovac [3]. These experiments, based on α-gating and two-detector coincidence techniques, respectively, have shown the importance of escape of primary photons undergoing single or multiple Compton scattering. However, these studies have not indicated any sign for the existence of a component due to photoelectron escape in the response function. Can [4] has recently investigated this problem without coincidence requirements, and observed two distinct components attributed to escape of photoelectrons and Compton-scattered photons.

Contrary to the case with Compton-scattered photons, escape of photoelectrons and Auger electrons has been investigated more extensively. Even though the main goal of these studies has been, for a long time, to determine the exponential tail and flat shelf on the low energy side of full-energy peaks, recent experimental investigations have revealed the existence of a shelf-like structure with definite cut-off energies corresponding to the binding energies of the detector material.

The earliest observation of the shelf structure was, to our knowledge, due to Campbell et al. [5], even though a flat shelf was also observed by Tikkanen et al. [6] and attributed to the escape of electrons to and from the contact layer. In the former study the Mn K X-ray spectrum using a ^{55}Fe source exhibited a shelf-like structure with cut-offs explained by the Si K-shell binding and X-ray energies. Papp et al. [7] studied the effect of the front contact materials on the response function of Si(Li) detectors for Mn K X-rays and demonstrated that certain spectral features are due to passage of electrons between different layers of the detector. Campbell et al. [8] extended these studies to variable energies in the range 1.8 - 8.3 keV. In that work Si(Li) and Ge detectors were used, and shelf structure was again observed with cut-off energies for Si K- and Ge L-shells. Furthermore, the response functions were also successfully reproduced by their Monte Carlo simulations. That study was expanded to the energy range 1-10 keV by Lepy et al. [9], and technologically improved Si(Li) and HPGe detectors were calibrated in the soft X-ray region by means of tunable monochromatized synchrotron radiation.

The gross features of low-energy X-ray spectrum (Mn K_α line at 5.9 keV) were studied both experimentally and analytically by Lowe [10]. Contribution of escape of photoelectrons and Auger electrons was calculated for appropriate shells and compared with the experimental response functions. The results showed that the calculated heights and shapes of electron escape steps were underestimated by about 15%. A close examination indicated that a cusp starting at the cut-off energy was expected with a long tail towards the full-energy peak (FEP).

The variations in response functions of several Si(Li) detectors were studied by Papp and Campbell [1]. It was shown that even the same detector might give slightly different response functions on different occasions. Nevertheless, the shelf structure was once again observed for 5.9 keV (Mn K_α). Campbell et al. [11] developed a model that incorporates Monte Carlo simulation, energy deposition by electrons, and an analytical approximation for diffusion of thermalized secondary electrons. The effects of contact, dead layer, range of electrons, and pulse processing time were studied in detail. In particular, the height of the steps were found to be strongly influenced by the pulse shaping time as an indication that these steps are due to electron escape from regions near the front surface.

Escape of X-rays of the detector material attracted much attention for almost two decades until escape of electrons and Compton-scattered photons was observed. The physical process for escape of characteristic X-rays is quite simple, and the energy of an escape peak in a spectrum is well defined. Nevertheless, escape peaks in a spectrum obtained in quantitative elemental analysis may overlap or even blend with the X-ray peaks of the sample material, and thus cause difficulty in determining peak positions and intensities.

One of the often-cited studies of Ge K_α and K_β escape as a function of energy is by Christensen [12] who obtained good agreement between measured and calculated relative intensities. Christensen's calculations were essentially based on an earlier work by Fioratti and Piermattei [13] who considered an infinite crystal and neglected Ge K_β escape. Seltzer's [14] analytical and Monte Carlo calculations showed good agreement with that work. Chan et al. [15] developed a Monte Carlo program to determine, among other things, K_α and K_β escape fractions, which confirm Seltzer's calculations. Recently, Can [16] studied the effect of collimator size on the escape of X-rays for 59.5 keV photons incident on an HPGe detector, and demonstrated the importance of escape from the side surface of the detector. In another recent work, Durak and Özdemir [17] measured escape fractions of K_α and K_β using X-rays from elements Zr to Yb in the energy range 15.75 - 52 keV for a Ge(Li) detector. A recent study by Campbell et al. [8] also demonstrated the importance of various components in the low-energy tailing of the full-energy peak in determining the line shape, energy and intensity of Si and Ge X-ray escape peaks.

An excellent review of Monte Carlo simulations, especially in the low-energy region [18-25], and for Si(Li) detectors was given by Campbell et al [11]. Several other works [1,14,15,26] deal with higher energy photons incident on Ge(Li) or HPGe detectors and should be mentioned. The information obtained from these simulations covers a wide range, from escape of characteristic X-rays to Compton-scattered escape profiles to escape of photoelectrons.

The above survey of the literature clearly demonstrates that while there has been a wide interest in the study of response functions for Si(Li) detectors in the low-energy region, the same is not true for Ge(Li) and HPGe detectors in the energy range of, say 10 - 60 keV. Even though the dominant interaction mechanism between a primary photon and a Ge atom was photoelectric absorption, which allowed us to study the effect of the escape of both Ge X-rays and photoelectrons, Compton-scattered photon escape was also observable.

It is for these reasons that we studied the response function of our HPGe detector in the energy range 8 - 52 keV using a variable-energy X-ray calibration source. Using Tb and Ba X-rays we clearly observed all three escapes mechanisms in the same experiment. However, for Ag, Mo, and Rb only X-ray and photoelectron escapes were observed. Finally, photoelectron escape for Cu was investigated for comparison with a similar work at 8 keV [8].

The fact that the primary X-ray beam was not monochromatic provided an advantage in measuring Ge X-ray escape by allowing us to study this mechanism at a large number of energies, but in the case of Compton and photoelectron escape, the stronger of the K_α and K_β X-rays was considered as the dominant contribution to these components of the response functions.

This thesis is organized as follows: in Chapter 2 the theory of interaction of radiation with matter is given. In Chapter 3 the experimental set-up, electronics and details of the source are given, and spectral features are discussed. In Chapter 4 the basic principles and details of the present application of the Monte Carlo simulation are given. Finally, in Chapter 5 the experimental results are presented and compared with the Monte Carlo simulations and other investigations.

CHAPTER 2

THEORY

2.1 Cross-section, Attenuation Coefficients and Mean Free Path

In this section we will discuss some concepts and give the definitions of the relevant fundamental quantities for the attenuation of a narrow photon beam through a material. Cross-section, σ, is defined as the effective area of a target particle for intercepting a photon or a unit of particle radiation, resulting in absorption or deflection of the incident radiation. Units of cross-section are cm^2 or b (barns), where 1 b = 10^{-24} cm^2. Total cross-section is given by the sum of the most probable individual processes by which photons interact with atoms

$$\sigma_{tot} = \sigma_{pe} + \sigma_{incoh} + \sigma_{coh} + \sigma_{pair} + \sigma_{trip} \qquad (2.1)$$

where σ_{pe} is the photoelectric absorption cross-section, σ_{incoh} and σ_{coh} are the incoherent (Compton) and coherent (Rayleigh) scattering cross-sections, respectively, and σ_{pair} and σ_{trip} are the cross-sections for electron-positron pair production in the field of the nucleus and in the field of the atomic electrons, respectively [27]. Since pair production has threshold above 1 MeV, it does not affect the X-ray spectroscopy energy region.

A quantity that is often referred to is X-ray linear attenuation coefficient, μ, defined as

$$\mu = N\sigma \tag{2.2}$$

in which N is the total number of target atoms per unit volume. Since μ depends on the density of the absorber through which the beam of photons attenuate, this dependence is removed by defining the mass attenuation coefficient

$$\mu/\rho\,(cm^2/g) = \sigma_{tot}\,(cm^2\,/\,atom)\,/\,[u(g)\,A] \tag{2.3}$$

where u (= 1.66x10^{-24} g) = $1/N_A$, (inverse of Avagadro's number) is the atomic mass unit, and A is the atomic mass of the target element.

A collimated photon beam of initial intensity I_0 after traversing a thickness x of absorber will have transmitted intensity, I, given by the exponential attenuation law

$$I = I_0\, e^{-(\mu/\rho)x}. \tag{2.4}$$

Finally, mean free path, λ, is defined as the distance over which the primary beam intensity is reduced by a factor 1/e, and is related to attenuation coefficient by

$$\lambda = \frac{1}{\mu}\,(cm). \tag{2.5}$$

2.2 Interaction of radiation with matter

There are four major processes for the interaction between the incoming photons and the target atoms: the photoelectric effect, Compton scattering, coherent (Rayleigh) scattering and the pair (and triplet) production. Among the other less-probable processes is photonuclear interaction that can induce radioactivity. The mass attenuation coefficient for the individual interactions and the sum of the former three processes for Germanium are shown in Figure 2.1 [28]. As we see, in the energy range (13.39 - 51.74 keV) considered in our studies, the major interaction is the photoelectric absorption while the total of the two scattering processes is about 20% of the total cross-section.

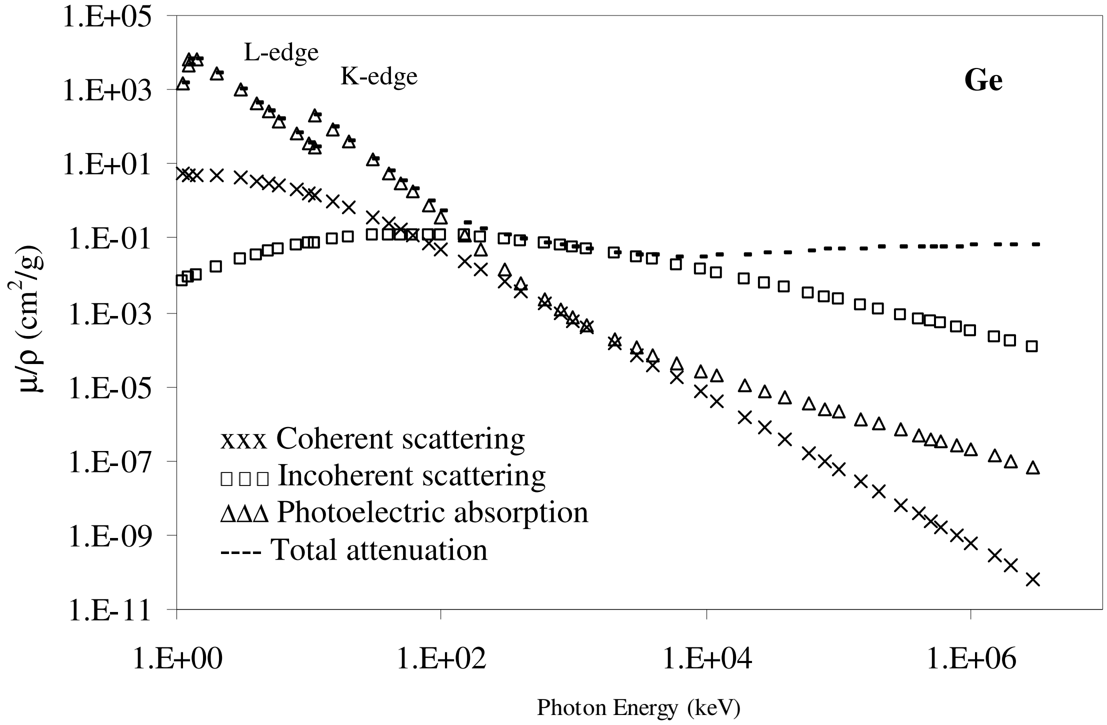

Figure 2.1: Mass attenuation coefficients for photons in Germanium.

The probability of a photon traversing a given amount of absorber without any kind of interaction is just the product of the probabilities of survival for each particular type of interaction.

2.2.1 Photoelectric Interaction

In the photoelectric absorption process, an incident photon interacts with an absorber atom in which the photon completely disappears and then an energetic electron is ejected by the atom from one of its bound shells as shown in Figure 2.2. The ejected electron is called a photoelectron. Below energies of about 100 keV the predominant mode of photon interaction in all medium and high Z absorbers is the photoelectric process.

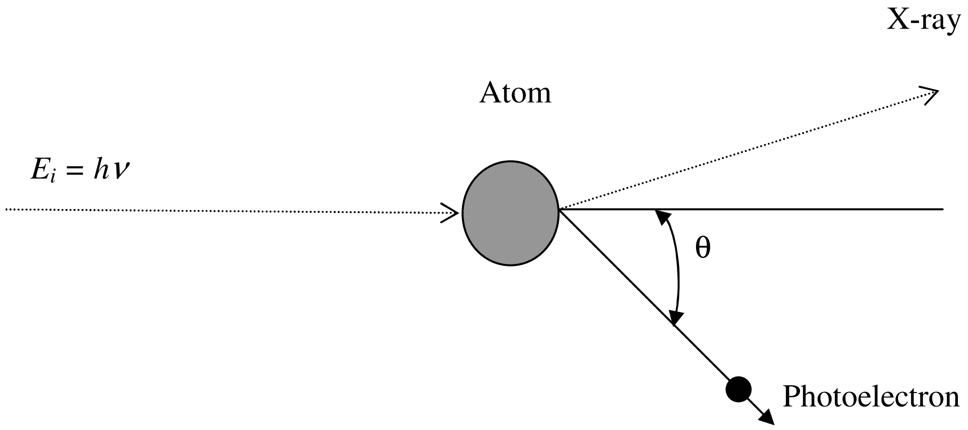

Figure 2.2: Photoelectric effect

An incident photon cannot be totally absorbed by a free electron. However, total absorption can take place if the electron is initially bound in an atom. Then the recoil of the entire residual atom conserves momentum. As might be expected, the most tightly bound electrons have the greatest probability of absorbing a photon, which is incident upon an atom. It is known both experimentally and theoretically that about 80 % of the photoelectric absorption process takes place in the K-shell, provided that the incident photon energy clearly exceeds the K-shell binding energy [29]. So the entire atom participates, the photoelectric process may be visualized as an interaction of the primary photon with the atomic electron cloud in which the entire photon energy, $E_i = h\nu$, is absorbed and an electron (usually K or L) is ejected from the atom with an energy

$$E_{pe} = E_i - E_K^{ab} \text{ (or } E_L^{ab}\text{)} \tag{2.6}$$

where E_K^{ab} is binding energy of the ejected electron. For example, in the case of 44.47 keV incident Tb $K_{\alpha 1}$ photons and K-shell of Ge $E_i^{K_{\alpha 1}}$ = 44.47-11.1=33.37 keV.

In addition to the ejection of a photoelectron, this process results in the isotropic emission of one or more fluorescence X-rays, due to an outer-shell electron filling the inner-shell vacancy created by the ejected photoelectron. The fluorescence X-ray energy is equal to the difference in binding energy between the participating inner and outer electron shells or subshells, hence a fluorescence X-ray spectrum consists of a number of discrete lines, each corresponding to one of many transition probabilities as shown in Figure 2.3.

The fluorescence X-rays do not necessarily emerge from the collided atom, but can instead dislodge outer electrons, similar in effect to a secondary photoelectric absorption. This additional emission of electrons is called the Auger effect, and emitted electrons are called Auger electrons. The probability that the primary fluorescence X-ray will escape from the atom without undergoing Auger processes is called the fluorescence yield, ω_i, in which i refers to the electron shell or subshell from which the primary photoelectron was removed [30].

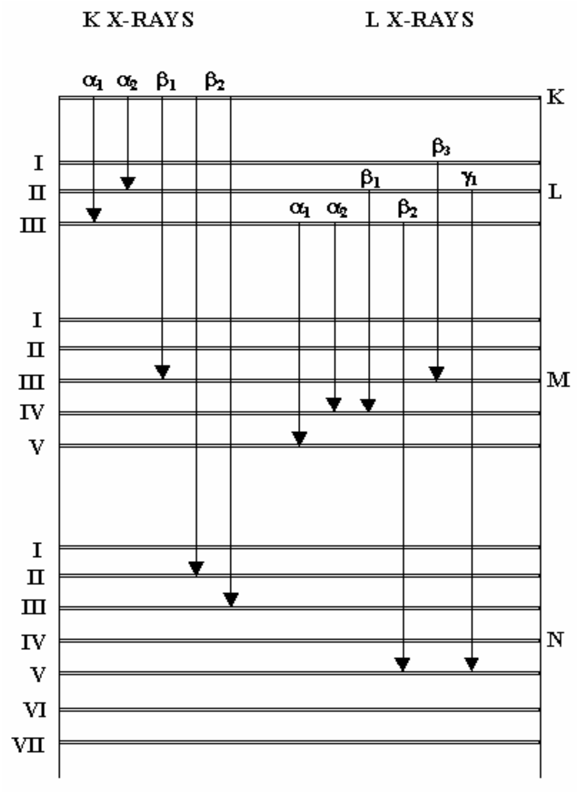

Figure 2.3: Atomic energy levels involved in the emission of K and L X-rays.

At low photon energies, the photoelectrons tend to be ejected in the direction of the electric vector of the incident radiation, hence at right angles to the direction of incidence. At higher energies, the angular distribution is more in the forward direction. The kinetic energy of the photoelectron, E_{pe}, is of course, the same for all directions of emission. The angular distribution of the photoelectrons for unpolarized, nonrelativistic photons is given as [31]

$$P(\theta) = k \sin^2 \theta \qquad (2.7)$$

where θ is the angle between the momentum vectors of the incident photon and the ejected photoelectron. As a photoelectron passes through matter it loses its energy in ionizing and radiative collisions. In addition, there is a large number of deflections due to elastic scattering.

The range, *R*, of an electron is an experimental concept relating to the thickness of an absorber, which the particle can penetrate. It must be recognized that the electron's total path length is a quantity, which is completely different from its range, as shown in Figure 2.4.

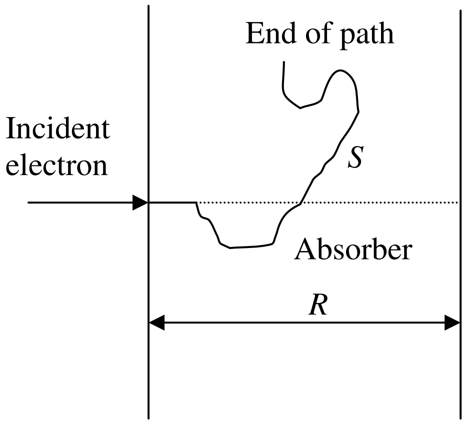

Figure 2.4: Schematic diagram of the path of an electron *S* and range *R*.

The total path length *S* is measured along the actual path of the electron, whereas the range *R* is the maximum distance reached in the initial direction of the electron.

The energy deposited within the absorber can be calculated by integrating the stopping power equation [32]

$$\frac{dE_{pe}}{dx} = R(\frac{MeV}{g}cm^2)\rho(\frac{g}{cm^3}) \tag{2.8}$$

where $$\frac{dE_{pe}}{dx} = \left(\frac{dE_{pe}}{dx}\right)_{coll} + \left(\frac{dE_{pe}}{dx}\right)_{rad} \tag{2.9}$$

The first term on the right side of Eq. (2.9) is due to collisional (excitation and ionization) energy loss given by

$$-\left(\frac{dE_{pe}}{dx}\right)_{coll} = \frac{2\pi e^4 NZ}{m_0 v^2}\left\{\begin{array}{l} \ln\frac{m_0 v^2 E_i}{2I^2(1-\beta^2)} - (\ln 2)(2\sqrt{1-\beta^2} - 1 + \beta^2) \\ \\ + (1-\beta^2) + \frac{1}{8}(1-\sqrt{1-\beta^2})^2 \end{array}\right\} \tag{2.10}$$

where

v	velocity of the primary particle

$\beta = v/c$

N	the number density,
Z	atomic number,
m_0	the electron rest mass
e	the electronic charge
I	the average excitation and ionization potential of the absorber
E_i	in units of MeV.

Electron may also lose its energy by radiative processes as well as by Coulomb interactions. These radiative losses take the form of Bremsstrahlung or electromagnetic radiation. We know classically that any charge must radiate energy when accelerated, and the deflections of the electron in its interactions with the absorber correspond to such acceleration. The second term on the right side of Eq. (2.9) is due to radiative energy loss and is given by

$$-\left(\frac{dE_{pe}}{dx}\right)_{rad} = \frac{NE_i Z(Z+1)e^4}{137 m_0{}^2 c^4}(4\ln\frac{2E_i}{m_0 c^2} - \frac{4}{3}). \tag{2.11}$$

The factors of Z^2 and E_i in the numerator show that radiative losses are most important for high electron energies and for absorbers of large atomic number.

It is interesting to note that the ratio of the specific energy losses is given by

$$\frac{\left(dE_{pe}/dx\right)_{rad}}{\left(dE_{pe}/dx\right)_{coll}} \cong \frac{E_i Z}{700} \tag{2.12}$$

For example, taking $E_i = E_{pe} = 0.0484$ MeV and Z = 32 for Ge, we see that the ratio is 0.0022 which clearly shows that at low energies energy loss is mainly due to collisions. When dE/dx is a slowly varying function, one can use Eq. (2.8) and the tabulated values of R [33] and evaluate the expected amount of energy loss ΔE by a photoelectron during its displacement Δx, or vice versa.

2.2.2 Compton Scattering

In Compton scattering, the incoming photon is deflected through an angle θ with respect to its original direction. The photon transfers a portion of its energy to the target electron, which is assumed to be initially at rest. The electron is known as a recoil electron. The probability of Compton scattering per atom of the absorber depends on the number of electrons available as scattering targets and therefore increases linearly with Z. The energy transferred to the electron can vary from zero to a large fraction of the photon energy because all angles of scattering are possible.

When the incident photon has an energy hν, which cannot be neglected in comparison with the rest mass energy, m_0c^2, of the electron a new and complicated set of phenomena occurs. This incident momentum must be conserved between the scattered photon and the struck electron. Except for the trivial case of zero scattering angle, the direction of the scattered photon is not parallel to the direction of the incident photon. The scattered photon must therefore have a smaller momentum, and hence a smaller quantum energy, than the incident photon. The remaining momentum and energy are imparted to the struck electron.

We shall first consider the case in which the struck electron is not only at rest, but is also unbound. In practice, this simply limits the theory to those cases for which the atomic binding energy of the struck electron is small compared with hν. Almost all practical cases fall within this region. If the photon energy is comparable with the binding energy of the atomic electrons, the photoelectric cross section usually greatly exceeds the Compton scattering cross section. In Figure 2.5 Compton scattering is illustrated schematically, where the paths of the incident and scattered photon define the scattering plane, and the path of the recoiling electron also lies in the same plane.

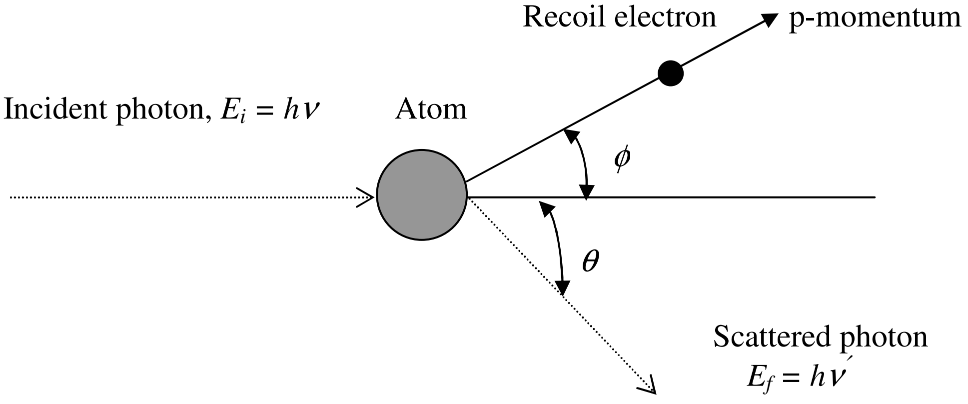

Figure 2.5: Compton Scattering

Using the momentum and energy conservations, we can write a relationship between initial and final photon energies in terms of the scattering angle θ as

$$E_f = \frac{E_i}{1+\alpha(1-\cos\theta)} \tag{2.13}$$

where $\alpha = h\nu/m_0c^2$ is a dimensionless parameter. For small scattering angles θ, very little energy is transferred. Some of the original energy is always retained by the incident photon, even in the extreme case of $\theta = \pi$. The kinetic energy of the recoil electron is therefore

$$E_{re} = E_i\left[\alpha(1-\cos\theta)/\left(1+\alpha(1-\cos\theta)\right)\right]. \tag{2.14}$$

Two extreme cases can be identified: First, If $\theta = 0$, the Eq. (2.14) predicts that $E_i \approx E_f$ and $E_{re} \approx 0$. In this case the recoil Compton electron has very little energy and the scattered photon has nearly the same energy as the incident gamma ray. Second, a head-on collision in which $\theta = \pi$. In this case the incident photon is backscattered toward its direction of origin, whereas the electron recoils along the direction of incidence. The maximum energy can be transferred to an electron in a single Compton interaction. For this case the Eq. (2.14) yields,

$$E_{re}\,|_{\theta=\pi} = E_i\left[\frac{2\alpha}{1+2\alpha}\right] \tag{2.15}$$

and energy of scattered photon is,

$$E_f \mid_{\theta=\pi} = \frac{E_i}{1+2\alpha} . \tag{2.16}$$

In normal circumstances all scattering angles will occur in the detector. Therefore, a continuum of energies can be tarnsferred to the electron, ranging from zero up to the maximum predicted by Eq. (2.15).

The angular distribution of scattered gamma rays is predicted by Klein-Nishina [34] formula for the differential scattering cross section $d\sigma/d\Omega$

$$\left(\frac{d\sigma}{d\Omega}\right)_{KN} = Zr_0^{\,2}\left\{\left(\frac{1}{1+\alpha(1-\cos\theta)}\right)^2\left(\frac{1+\cos^2\theta}{2}\right)\left(1+\frac{\alpha^2(1-\cos\theta)^2}{(1+\cos^2\theta)(1+\alpha(1-\cos\theta))}\right)\right\} \tag{2.17}$$

where r_0 is the classical electron radius.

However, the initial momentum distribution of bound electrons must be taken into account. The energy E_f of the photon after the scattering is related to the component of electron momentum parallel to the scattering vector by the following expression [35,36]

$$p_z = \frac{E_i E_f (1-\cos\theta) - m_0 c^2 (E_i - E_f)}{c(E_i^{\,2} + E_f^{\,2} - 2E_i E_f \cos\theta)^{1/2}} \tag{2.18}$$

which may be used together with the Compton profile [37], *J(Q)*, in order to find E_f orresponding to E_i, p_z, and θ. Here $Q = -\mathbf{k}.\mathbf{p}/k$ and $\mathbf{k}$ is the momentum transferred to the electron. Compton profile of Germanium is shown in Figure (2.6).

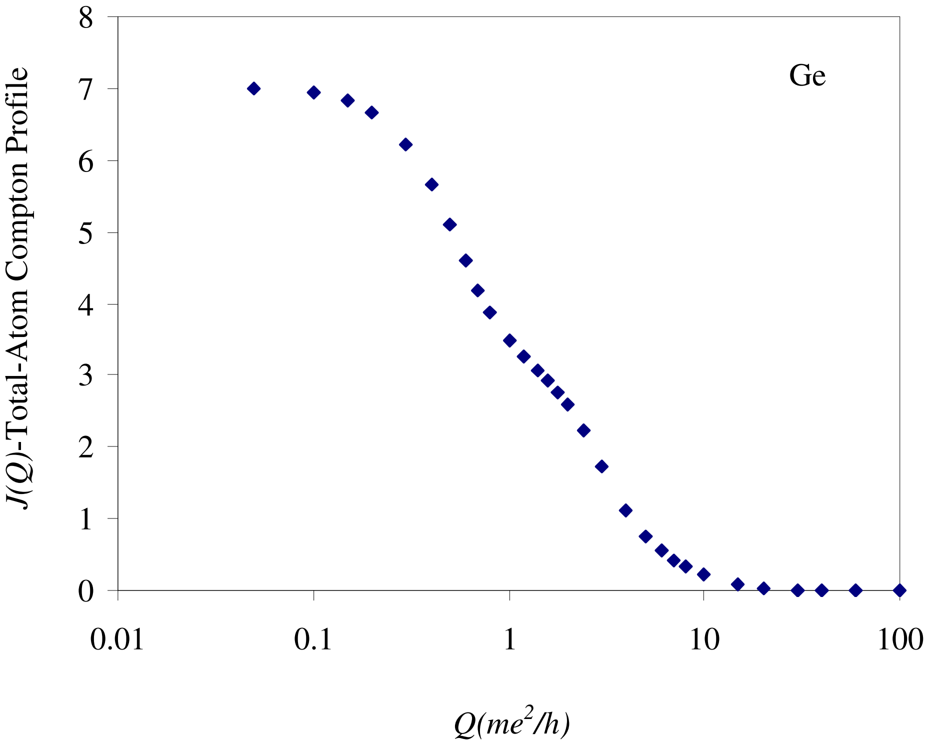

Figure 2.6: Total-atom Compton profile

At lower energies, say $E_i < 100$ keV the Klein-Nishina cross-section needs to be modified for electron binding using the incoherent scattering function $S(E_i, \theta, Z)$ [38,39] reduces the cross-section for small momentum transfers for low-angle scattering

$$\left[\frac{d\sigma}{d\Omega}\right]_{incoh} = \left[\frac{d\sigma}{d\Omega}\right]_{KN} \cdot S(E_i, \theta, Z)\,. \qquad (2.19)$$

2.2.3 Coherent Scattering

Coherent (Rayleigh or elastic) scattering is the process by which photons are scattered by bound atomic electrons without excitation of the target atom, i.e. the energies of the incident and scattered photons are the same. Even at energies of 0.1 MeV and above, elastic coherent scattering by tightly bound atomic electrons can be significant in heavy elements. The permissible Rayleigh scattering angles are always small, because the recoil imparted to the atom must not produce atomic excitation or ionization.

When the energy of the incident photon is small compared to the electron rest energy, one can write $E_f = E_i$ and Klein-Nishina formula reduces to the Thomson expression [40] for elastic scattering

$$\left(\frac{d\sigma}{d\Omega}\right)_{Th} = \frac{r_0^{\ 2}}{2}\left(1+\cos^2\theta\right). \tag{2.20}$$

Due to the finite size of the atom, coherent scattering cross-section needs to be corrected by the form factor $F(x, Z)$ [39],

$$\left(\frac{d\sigma}{d\Omega}\right)_{Th} = \frac{r_0^{\ 2}}{2}\left(1+\cos^2\theta\right)\cdot\left[F(x,Z)\right]^2 \tag{2.21}$$

in which x is a momentum transfer variable related to the incident photon energy E_i and its subsequent deflection angle θ, and Z is the atomic number of the target atom.

2.2.4 Pair Production

In this interaction, an incident photon with a minimum energy of 1.02 MeV (i.e. 2 times m_0c^2) collides with a nucleus and an electron-positron pair is created. In this process, the photon is completely absorbed and in its place appears a electron-positron pair whose total energy is equal to E and we can write

$$E_i = (T_- + m_0c^2) + (T_+ + m_0c^2) \tag{2.22}$$

where T_- and T_+ are the kinetic energies of the electron and positron, respectively [41]. In these experiments, the photons had maximum energy of 51.74 keV. Therefore, pair production process was not possible.

CHAPTER 3

EXPERIMENT

3.1 Experimental Setup

The experimental setup is shown in Figure 3.1. The photon source was located 65 mm above the detector on its main axis. The distance between the front surface of the detector and the Beryllium window was 5 mm.

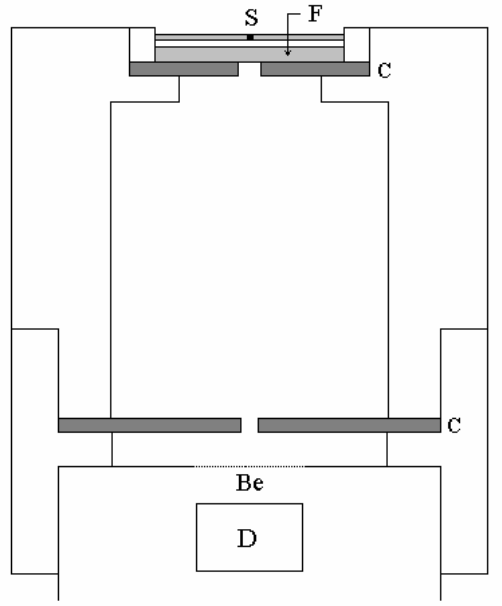

Figure 3.1: Experimental setup (F: Filter, S: Source, C: Collimator, D: Detector, Be: Beryllium window) (not to scale).

Two lead collimators (2 mm thick), located at the bottom and at the top of the brass source holder, were used. The top collimator was used to minimize the number of photons reaching the detector after being scattered from the source holder, while the bottom collimator defined the desired solid angle. An Al filter with 0.5 mm thickness was placed directly under the source in order to filter out, whenever necessary, the low energy L X-rays from the point source.

3.2 Details of the Source

A variable-energy calibration source (Amersham, code AMC. 2084) was used. Photons with 59.5 keV energy from an ^{241}Am point source were used to excite the target elements Rb, Mo, Ag, Ba, and Tb in the calibration source. The excited elements produced X-rays in the energy range ~13.39 – 51.74 keV. The most commonly seen X-ray lines are given in Table 3.1, where K_{ab} is the binding energy of the K-shell electron. The most probable X-rays $K_{\alpha 1}$, $K_{\alpha 2}$, $K_{\beta 1}$, and $K_{\beta 2}$ are shown in Figure 2.3. The energies of the source X-rays are given in Table 3.2.

Table 3.1: Prominent lines in X-ray fluorescence

Line	Transition
$K_{\alpha 1}$	$L_3 \rightarrow K$
$K_{\alpha 2}$	$L_2 \rightarrow K$
$K_{\beta 1}$	$M_3 \rightarrow K$
$K_{\beta 2}$	$N_2, N_3 \rightarrow K$

Table 3.2: The energies of the source X-rays

	E_i (keV)			
	$E_i^{K_{\alpha 1}}$	$E_i^{K_{\alpha 2}}$	$E_i^{K_{\beta 1}}$	$E_i^{K_{\beta 2}}$
Rb	13.39	13.34	14.96	15.13
Mo	17.48	17.37	19.60	19.96
Ag	22.16	21.99	24.94	25.45
Ba	32.19	31.82	36.38	37.26
Tb	44.47	43.74	50.40	51.74

3.3 Germanium Detector Characteristics

A planar high-purity Germanium detector (HPGe) was used in our experiments. Configuration of a planar HPGe detector is shown in Figure 3.2. The detector (Canberra, Model 3502) had 10 mm thickness, 16 mm active diameter and 200 mm^2 active area.

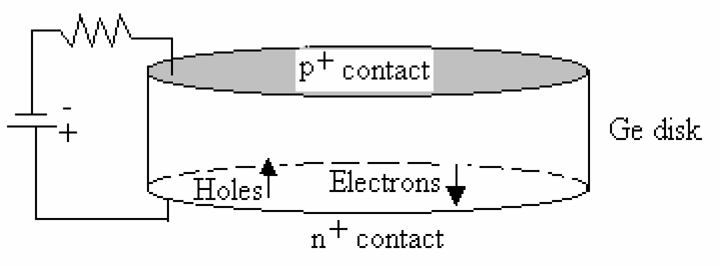

Figure 3.2: Configuration of the HPGe detector

When radiation falls on the crystal, electron-hole pairs are produced. These are collected by the electrods and a signal is obtained across the resistance. The signal is amplified and used to charge a capacitor. The discharging time of the capacitor designates the energy channel in which the event is recorded.

The most important property of semiconductor detectors is their favorable energy resolution which depends on number of electron-hole pairs produced by the radiation. The electron-hole pairs should be free to move in the detector and reach the electrods. The energy resolution depends partly on the noise sources in the detector and on the charge collection. If the detector contain traps produced by crystal defects and impurities, the electrons are captured by them before reaching the electrods. High-purity detector material is used in order to minimize this problem. Complete charge collection is obtained by ensuring a large electric field over the sensitive detector volume, while detector noise contributions mainly result from surface leakage current. The prevention of recombination and trapping and extent of the surface leakage current thus depend on the bias voltage applied to the detector. In our experiment we applied –500 V to our detector.

Due to the large thermal generation rate of hole-electron pairs by excitation of electrons across the band gap, operation of germanium detectors at room temperature is impossible. So we used liquid-nitrogen to cool the system.

3.4 Electronics

Standard electronic equipment and pulse-processing units were used as shown in Figure 3.3.

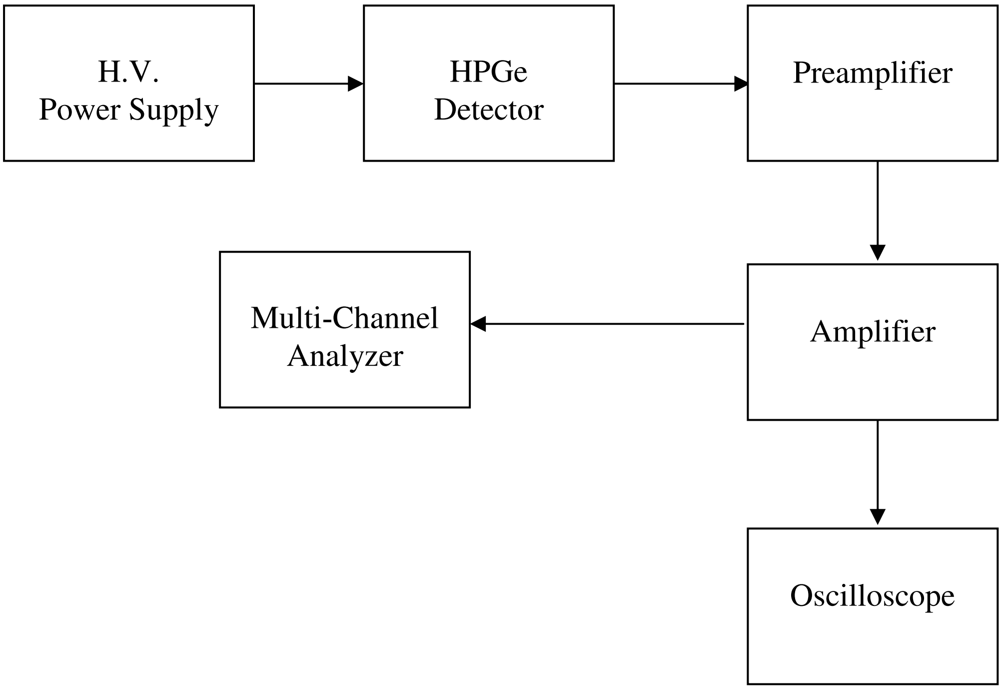

Figure 3.3: Electronic equipment

3.4.1 Preamplifier

When the liberated charge by the incident radiation is small, it is impractical to deal with the signal pulses without an intermediate amplification step. The first part in a signal-processing chain is, therefore, often a preamplifier as an interface between the detector and the pulse-processing. One function of the preamplifier is to terminate the capacitance quickly and therefore to maximize the signal-to-noise ratio. The preamplifier provides no pulse shaping, and its output is a linear tail pulse. The rise time of the output pulse is kept as short as possible, consistent with the charge collection time in the detector itself. The decay time of the pulse is made quite large, so that full collection of the charge can occur.

3.4.2 Amplifier

Amplifier input-port is connected to the signal source, which produces the signal as some low-amplitude, low-power time function. The device delivers the same signals, at higher amplitude and power level, to a load connected to its output port. The main amplifier amplifies the signals in order to be ready for the multi-channel pulse height analyzer to rearrange the pulse height of the peaks.

3.4.3 Analogue-to-Digital Converter (ADC)

ADC is based on the conversion of a pulse of given amplitude into a number of equal time intervals by means of a clock pulse generator. The input signal is first lengthened by means of a suitable pulse stretching circuit. When the pulse amplitude reaches its maximum value, a capacitor can be charged which is then linearly discharged. Simultaneously, a linearly rising waveform and a clock oscillator is started. At the moment the voltage of both pulses becomes equal, the clock oscillator is disconnected. The number of clock pulses during the time interval is proportional to the original pulse amplitude. These time intervals can be counted with a high precision, and each number is allocated to one channel. The time for discharge is then used as a measure for the pulse amplitude (i.e. photon’s energy).

3.5 Spectral Features

The interaction mechanisms of X-rays with the detector material are shown in Figure 3.4, where only the escape routes through the front surface were indicated.

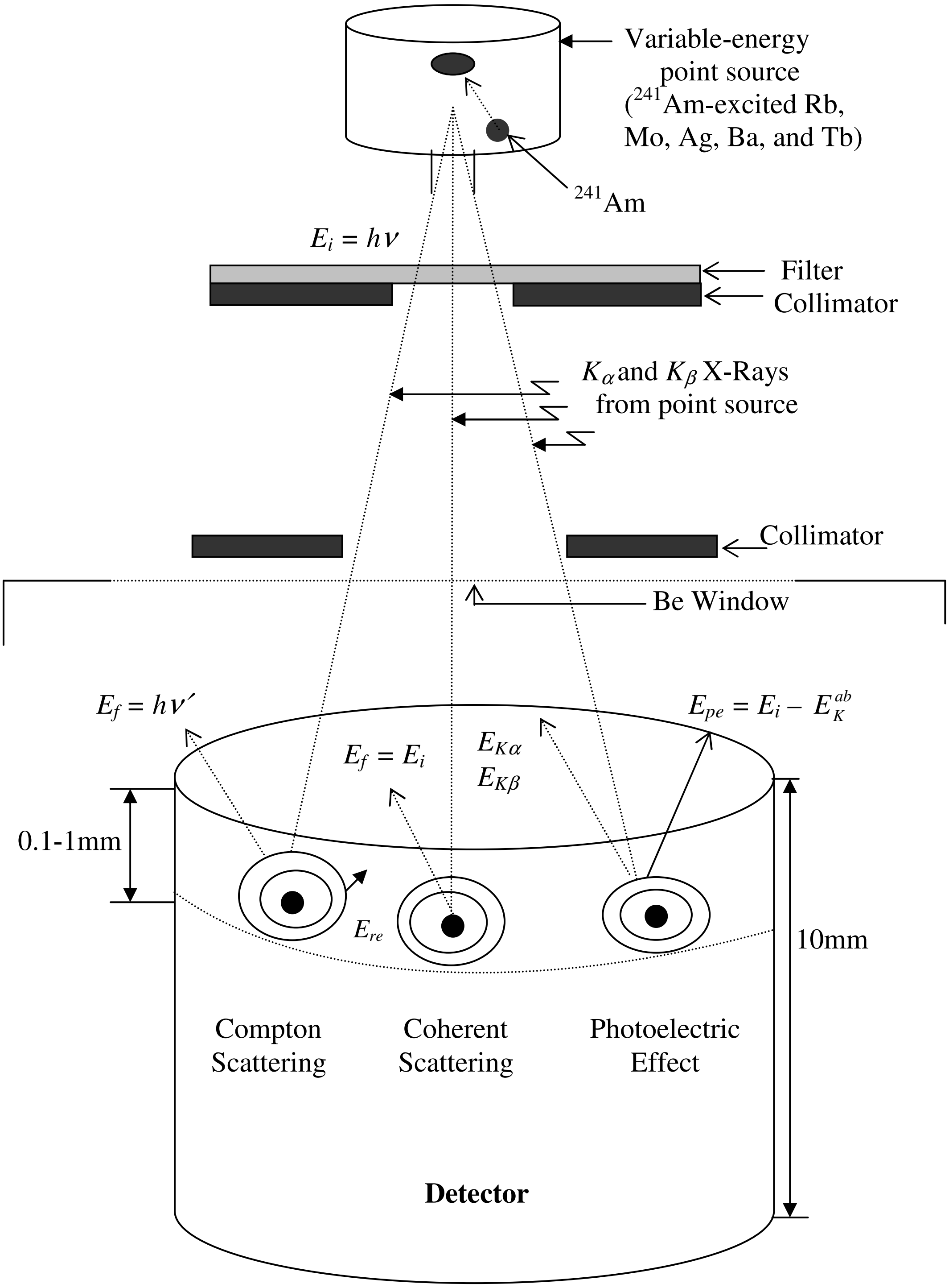

Figure 3.4: Interaction mechanisms of X-rays with Ge atoms (not to scale)

In order to illustrate the features due to major interactions of incident photonswith the detector a pulse height spectum is given in Figure 3.5.

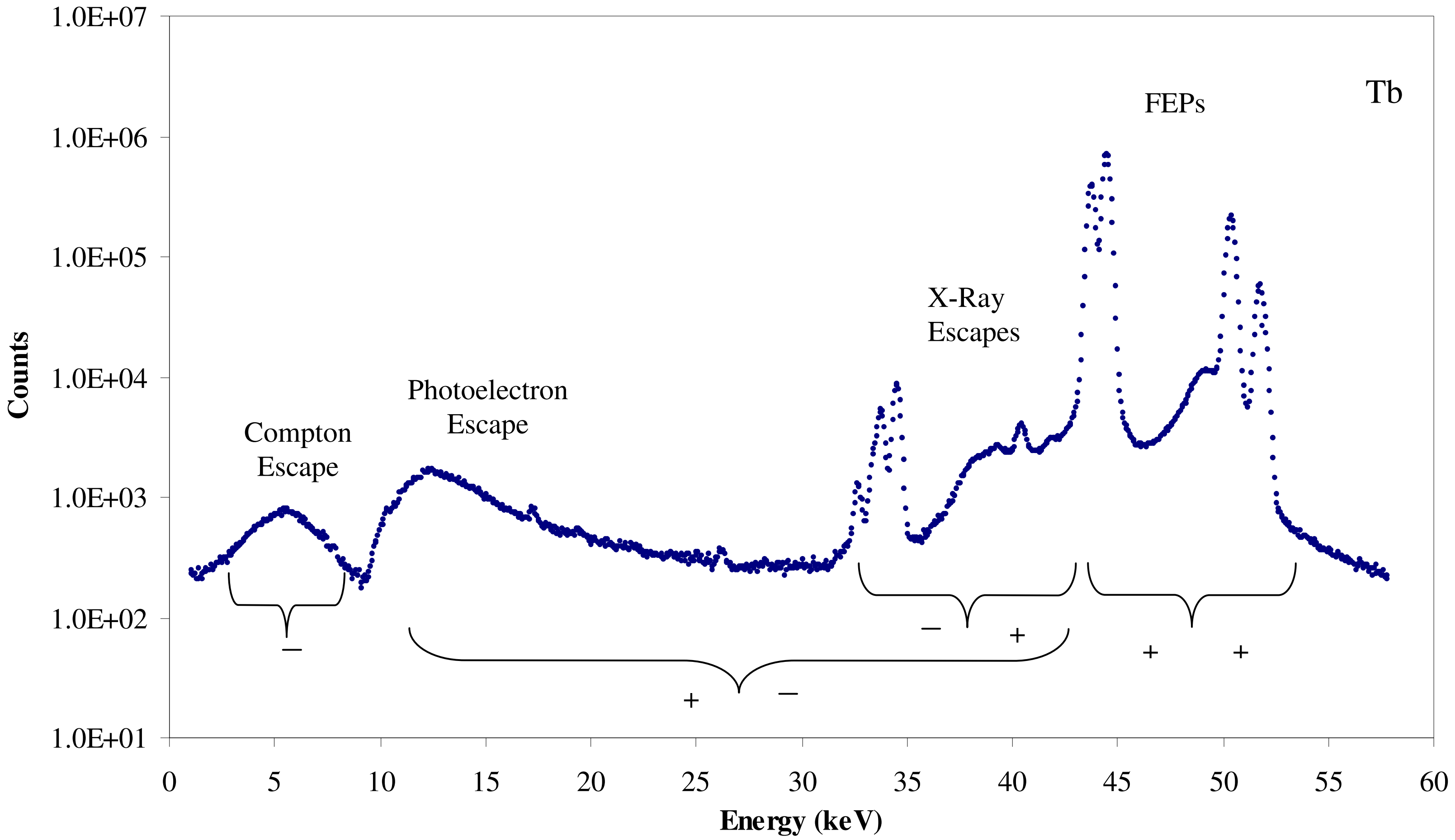

Figure 3.5: Typical spectrum showing FEP's and all the escape events.

The full-energy peaks and the escape peaks/distrubutions in Figure 3.5 are best explained in terms of “escape” and/or “absorption” labeled as (-) and (+), respectively as presented in Table 3.3.

Table 3.3: Analysis of the spectrum

Primary photon	X-Ray	Photoelectron	Event
	+	+	FEPs
	-	+	X-Ray escape
	+	-	Photoelectron escape with energy range (E_K^{ab} or $E_L^{ab} - E_i$) keV
-			Compton or coherent escape

3.5.1 Full-Energy Peaks

Some of the incident photons interact with the germanium atoms and lose all or part of their energy in atomic processes. Ideally, an incoming photon is expected to deposit all of its energy into the detector. This event is described by (++) namely, both photoelectron and Ge X-ray, produced by incident photon, were absorbed. In this case the full-energy peaks (FEPs) are obtained as shown in Figure 3.5. Each peak is defined by the α or β label according to its origin.

It should be noted that for Cu, Rb and Mo X-rays $K_{\alpha 1}$ and $K_{\alpha 2}$, and $K_{\beta 1}$ and $K_{\beta 2}$ peaks are close together in energy because of the limited energy resolution of the detector. They were observed as two peaks which we labeled K_α and K_β.

The full width at half maximum (FWHM) is defined as the width of the distribution at a level that is just half the maximum ordinate of the peak. The energy resolution of the detector is conventionally defined as the FWHM divided by the energy of the peak centroid. The energy resolution is thus a dimensionless fraction conventionally expressed as a percentage. It should be clear that the smaller the figure for the energy resolution, the better the detector will be able to distinguish between two radiations whose energies lies near each other. The dominant characteristic of germanium detectors is their excellent energy resolution. In this experiment, the FWHM values of $K_{\alpha 1}$, $K_{\alpha 2}$, $K_{\beta 1}$, and $K_{\beta 2}$ peaks of Tb X-rays were 0.39, 0.39, 0.45, and 0.46 keV, respectively.

3.5.2 Ge X-Ray Escape

Characteristic X-ray escape event is described by (– +). That is, Ge X-ray escapes but the photoelectron ejected during the photoelectric interaction remains (loses its energy) inside the detector. In this case the Ge X-ray escape peaks are obtained as shown in Figure 3.5. If the resolution is good, two escape peaks are observed for each FEP. The energies of the escape peaks correspond to $E_i - E_{K\alpha}$ and $E_i - E_{K\beta}$, where E_i is the initial energy of the photon and $E_{K\alpha}$ and $E_{K\beta}$ are the energies of Ge K_α and K_β X-rays.

In our investigations, the energy range of X-ray escape peaks was between 3.5 keV and 40.7 keV. A complete list of the energies of X-ray escape peaks for the incident photons are given in Table 3.4., regardless of the resolution obtained at a particular energy.

Table 3.4: Energies of X-ray escape peaks (in keV)

	$E_i^{K_{\alpha1}}$		$E_i^{K_{\alpha2}}$		$E_i^{K_{\beta1}}$		$E_i^{K_{\beta2}}$	
	$E_{K\alpha}$	$E_{K\beta}$	$E_{K\alpha}$	$E_{K\beta}$	$E_{K\alpha}$	$E_{K\beta}$	$E_{K\alpha}$	$E_{K\beta}$
Rb	3.5	2.4	3.5	2.4	5.1	4.0	5.3	4.1
Mo	7.6	6.5	7.5	6.4	9.7	8.6	10.0	9.0
Ag	12.3	11.2	12.1	11.0	15.1	14.0	15.6	14.5
Ba	22.3	21.2	22.0	20.8	26.5	25.4	27.4	26.3
Tb	34.6	33.5	33.9	32.8	40.5	39.4	41.8	40.7

3.5.3 Compton Escape

This event is described by (-) in Table 3.3 where (-) describes escape of primary X-ray after Compton scattering. Compton interaction is purely a kinematic collision between the photon and an electron in the crystal that is either free or loosely bound as seen in Figure 2.5. Incoming photon pass through detector in some depth and scatters from a free or loosely bound electron after single (or multiple) interaction. The most probable way to escape is through a conical region around 180^0, namely, after bouncing off the electron. The recoil electron is assumed to be absorbed locally. The energy of the recoil electron can be calculated by semi-emprical formula which was given in Chapter 2 for free electron. In our experiment, the energy range of the recoil electrons is between 1.1 - 8.7 keV. Compton escape peaks could not be observed for low-Z elements like Mo and Ag, in this experiment, since Compton interaction has much smaller probability at the lower energies. The energy of Compton electrons and Compton X-ray escapes are given in the Table 3.5.

Table 3.5: The energies of Compton recoil electrons and Compton-scattered X-rays for 180-degree scattering (in keV).

	Compton recoil electrons				Compton-scattered X-rays			
	$E_{re}^{K_{\alpha 1}}$	$E_{re}^{K_{\alpha 2}}$	$E_{re}^{K_{\beta 1}}$	$E_{re}^{K_{\beta 2}}$	$E_{f}^{K_{\alpha 1}}$	$E_{f}^{K_{\alpha 2}}$	$E_{f}^{K_{\beta 1}}$	$E_{f}^{K_{\beta 2}}$
Mo	1.1	1.1	1.4	1.5	16.4	16.3	18.2	18.5
Ag	1.8	1.7	2.2	2.3	20.4	20.3	22.7	23.2
Ba	3.6	3.5	4.5	4.7	28.6	28.3	31.9	32.5
Tb	6.6	6.4	8.3	8.7	37.9	37.3	42.1	43.0

3.5.4 Photoelectron Escape

Finally, this event is described by (+ –), namely, the photoelectron escapes but Ge X-ray is absorbed. Incoming photon enters the detector and interacts primarily with the bound Ge K-shell electrons. Essentially, the photon gives all of its energy to the bound electron and knocks it out of the atom with an energy $E_{pe} = E_i - E_K^{ab}$. Since E_K^{ab} is about 11.1 keV for the Ge K-shell, we can see that the photoelectron has most of the energy. The energies of the photoelectrons for the incoming photons are given in Table 3.6. The photoelectron can loss its energy by either radiation or collision process according its energy. Figure 3.6 shows that the photoelectrons with energies in the range 6.4 - 40.6 keV lose their energies mainly by inelestic collisions in the detector.

Table 3.6: The energies of photoelectrons

	E_{pe} (in keV)			
	$E_{pe}^{K_{\alpha 1}}$	$E_{pe}^{K_{\alpha 2}}$	$E_{pe}^{K_{\beta 1}}$	$E_{pe}^{K_{\beta 2}}$
Mo	6.4	6.3	8.5	8.9
Ag	11.1	10.9	13.8	14.4
Ba	21.1	20.7	25.3	26.2
Tb	33.4	32.6	39.3	40.6

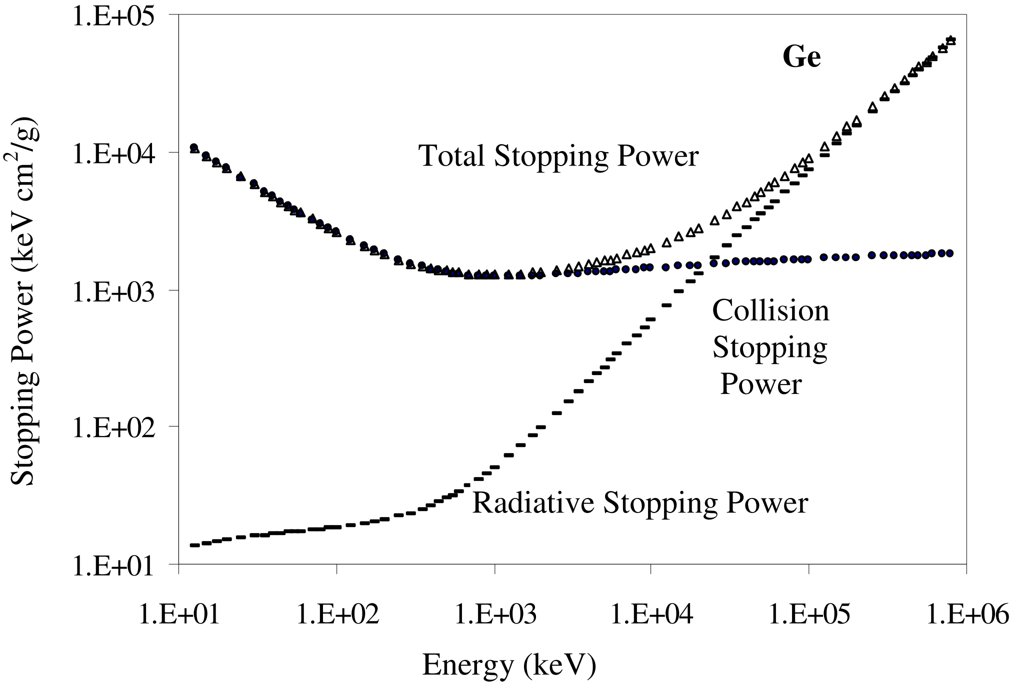

Figure 3.6: Stopping power for electrons

The photoelectron leaves almost all or part of its energy in the detector during this process. So, photoelectron escape distributions stretch out from 11.1 to 40.6 keV as seen in the Figure 3.5. The distribution (spectrum) is highly asymmetric which is represented by a Gaussian function on the low-energy side, but with an exponential on the high-energy side.

CHAPTER 4

MONTE CARLO SIMULATION

The principle of Monte Carlo method is based on simulating a great number of individual photons passing through detector material [42]. If one knows all relevant probabilities for the atomic interactions in the "life history" of a photon, the Monte Carlo method can be applied to predict the outcome of these processes. The program followed the history of a large number of photons from each target element. The output was tested for the effect of the number of incident photons and an optimum value of 10^6 was obtained. On a Pentium III (450 MHz) computer, typical run time was about 45 minutes.

A photon is characterized by its energy, position and direction coordinates. Space coordinates (x, y, z) were used for position of each photon together with direction cosines (u, v, w) for its direction of flight:

$$u = \cos\alpha \tag{4.1a}$$

$$v = \cos\beta \tag{4.1b}$$

$$w = \cos\gamma \tag{4.1c}$$

where $\pi \geq \alpha, \beta, \gamma \geq 0$ and

$$1 \geq u, v, w \geq -1 .$$

Note that $$u^2 + v^2 + w^2 = 1 . \tag{4.2}$$

In order to determine the location of the first collision, we make use of the attenuation law

$$dn = -nN\sigma(dl) \tag{4.3}$$

for a beam of n_0 particles. Eq. (4.3) has the solution

$$n = n_0 \exp(-N\sigma l) \tag{4.4}$$

where *n* is the number of particles remaining in the beam after traversing a distance l in the detector material. It is supposed that

$$P(l)dl = [\exp(-N\sigma l)]N\sigma(dl) \tag{4.5}$$

is the probability for a first collision between l and $l + dl$, and

$$P(l) = \int_0^l \exp(-N\sigma l)N\sigma(dl) = 1 - \exp(-N\sigma l) \tag{4.6}$$

is the probability distribution function for a first collision at distance $\leq l$. It follows that the Monte Carlo determination of distance l from an arbitrary point of departure to first collision, assuming the detector material homogeneous and infinite must be

$$r = P(l) = 1 - \exp(-l/\lambda) \tag{4.7}$$

where r is a random number defined in the same interval as P(l), i.e. $0 \le r \le 1$. Thus l can be written as

$$l = -\lambda \ln(1\text{-r}). \tag{4.8}$$

Since 1-r is equidistributed on $0 \le r \le 1$, we may use simply

$$l = -\lambda \ln \text{r}. \tag{4.9}$$

Eq. (4.9) was used not only to determine the location of the first collision from the front surface of the detector, but also to find the distance between successive collisions.

The final direction parameters (i.e. direction cosines) of a Ge X-ray or a scattered-photon in the laboratory system were given by

$$u' = \frac{(bcwu - bdv)}{\sqrt{(1-w^2)}} + au \tag{4.10a}$$

$$v' = \frac{(bcwv + bdu)}{\sqrt{(1-w^2)}} + av \tag{4.10b}$$

$$w' = -bc\sqrt{(1-w^2)} + aw \tag{4.10c}$$

where u, v and w are the direction cosines of the incident line of flight (Eqs. 4.1a, 4.1b, and 4.1c), and

$$a = \cos\phi \tag{4.11a}$$

$$b = \sin\phi = \sqrt{(1 - a^2)} \tag{4.11b}$$

$$c = \cos\delta \tag{4.11c}$$

$$d = \sin\delta = (sign \text{ of } \delta)\sqrt{(1 - c^2)} \qquad -\pi \le \delta \le \pi \tag{4.11d}$$

where ϕ is the scattering angle (or emission angle for the Ge X-rays) with direction of the incident line of flight, and δ is the azimuthal angle uniformly distributed on $-\pi \le \delta \le \pi$.

When $|w|$ is too close to unity, the following equations are used:

$$u' = bc \tag{4.12a}$$

$$v' = bd \tag{4.12b}$$

$$w' = aw\,. \tag{4.12c}$$

When the new direction cosines for the scattered photon (or emitted X-ray) are found, the location of the next interaction can be found by

$$x' = x + u'l \tag{4.13a}$$

$$y' = y + v'l \tag{4.13b}$$

$$z' = z + w'l \tag{4.13c}$$

where l is given in Eq. (4.9).

In the case of the point source the initial direction and point of entrance of the photon into the detector were determined by random sampling from the uniform distribution within the range allowed by the collimator. First the coordinates of the entrance point into the detector were found, and then the mean free path of the photon in Ge [14, 29, 43] was used, along with a random number, to determine the location of the first interaction. If the location of the first interaction of the gamma ray is outside the detector the photon is presumed to escape without interaction and the history of the photon is terminated. On the other hand, if the location of the first interaction is inside the detector the photon is assumed to have undergone an interaction.

The types of interactions considered for the photons with a Ge atom were the photoelectric effect, Compton scattering and coherent scattering. Using the corresponding cross-sections [29] and a random number the type of the first (second, third etc.) interaction was determined.

In the case of photoelectric effect, the history of K_α or K_β X-rays, having the energies of 9.876 keV and 10.983 keV with relative intensities of 0.884 and 0.116 [29] were followed, assuming isotropic emission. If a K_α X-ray, with the mean free path of 45 μm, or a K_β X-ray, with the mean free path of 60 μm was still inside the geometrical boundaries of the detector, it was assumed to be absorbed, and a full-energy peak event was registered. Otherwise, an event for K_α and K_β escape was recorded. All other X-rays from higher shells and Auger electrons were assumed to be absorbed completely due to small mean free paths.

The history of the photoelectrons was followed using the angular distribution that is proportional to $\sin^2\theta$ for nonrelativistic electrons [31]. The photoelectrons that escaped from the detector were recorded regardless of the amount of energy deposited prior to escape.

In the case of an inelastic scattering, that is the Compton effect, the angle of scattering was determined using the Klein-Nishina differential cross-section formula corrected by the scattering factor, Eq. (2.19), along with a random number. Using the scattering angle and the azimuthal angle, chosen randomly from a uniform distribution, the new direction of the photon and the location of the next interaction were determined. If the interaction point was outside the detector, the incident photon was said to have escaped after depositing only a part of its energy. If, on the other hand, the photon was still within the detector, the second interaction, at the new energy obtained from Eq. (2.18), was considered. The recoiling electron was assumed to be absorbed locally.

Finally, in the case of elastic scattering, the angle was determined randomly from the Thomson cross-section corrected by the form factor, Eq. (2.21).

CHAPTER 5

DISCUSSION AND CONCLUSIONS

The pulse-height distributions, i.e. spectra, of Tb, Ba, Ag, Mo, Rb, and Cu are presented in Figs. 5.1-5.6. All spectra were analyzed using a peak-fitting program (Jandel Scientific, 1989). In the case of spectra with adequate resolution all FEPs, i.e. $K_{\alpha 1}$, $K_{\alpha 2}$, $K_{\beta 1}$ and $K_{\beta 2}$, and their escape peaks were fitted by individual Gaussian distributions. Otherwise, X-ray lines with energies that are very close to each other, for example $K_{\alpha 1}$ and $K_{\alpha 2}$, were represented by a single peak centered at the weighted-average energy. Compton-escape was represented, approximately, by a Gaussian distribution. Exponentially modified Gaussian distribution was used to find the area under the photoelectron escape component. Figures 5.7-5.11 show the details of the peak-fitting procedure for various parts of Ba spectrum.

5.1 X-Ray Escape Fractions

X-Ray escape fractions, $P_{X\alpha} = I(K_{\alpha})/I(\mathrm{FEP})$ and $P_{X\beta} = I(K_{\beta})/I(\mathrm{FEP})$, as a function of the incident photon energy are given in Table 5.1. We compared our results with other analytical calculations and Monte Carlo simulations [14,15], which were in good agreement with the earlier measurements [12]. Also given in Table 5.1

are the results of a recent study [17], which are generally higher than the rest. We believe this was because of detector efficiency corrections, which were not needed. Table 5.1 also gives the results of our recent [4] experiments and Monte Carlo calculations at 59.54 keV (^{241}Am). As can be seen, the ratios $P_{X\alpha}$ and $P_{X\beta}$ both decrease with increasing incident energy. This can be attributed to the fact that while the mean free paths of Ge X-rays remain the same (45μm for K_α and 60 μm for K_β), the depth at which they originate increases from 15 μm to 600 μm with increasing energy. A close examination of Table 5.1 shows that the agreement between our results and other experimental and Monte Carlo studies is very good.

5.2 Compton Escape Fractions

Escape of incident photons following Compton scattering was observed for Tb and Ba with rather broad distributions centered at about 5.3 keV and 3 keV, respectively. These energies correspond to escape of incident photons after a 180-degree scattering, as expected, since it allows the shortest path for escape. Table 5.2 gives the experimental escape fractions, P_{com} = I(Compton)/I(FEP), along with Monte Carlo calculations, as well as the results at 59.54 keV [4] and of other works [2,15]. Contrary to the case with X-ray escape fractions, we were able to give only the total counts under the escape component divided by the total area under all FEPs. The decrease in the ratio as a function of decreasing energy was expected since the photoelectric cross-section becomes larger compared to that of Compton scattering. The agreement between measured fractions and the Monte Carlo simulations was quite good.

5.3 Photoelectron Escape Fractions

Perhaps the most interesting part of this study was the escape of photoelectrons originating from K-shell and/or L-shell of Ge depending on the energy of the incident photons. Figure 5.1, 5.2 and 5.3 show the photoelectron escape component of the response function for the incident Tb, Ba, and Ag K X-rays. In the case of Ge K-shell photoelectrons with ranges 6.7 μm, 3.2 μm, and 0.2 μm [33,44] for Tb, Ba, and Ag, respectively, the distribution due to partial deposition of energy is expected to start at about 11 keV and extend up to the FEPs. The cut-off corresponds to the energy of Ge K_{abs}.

In the case of incident Mo and Rb X-rays, Figure 5.4 and 5.5, the distribution due to escape of Ge K-shell photoelectrons is obscured by the tail due to escape of Auger electrons and incomplete charge collection, while the role of L-shell photoelectrons becomes evident. L-shell photoelectron escape is seen in the Mo spectrum, starting at the L-shell edge energy (about 1.2 keV) of Ge. There is also a clear indication of such a distribution for Rb just below the X-ray escape peaks. Figure 5.6 shows Cu spectrum which was taken for the purpose of comparison with ^{55}Fe (Mn X-rays) spectrum studied by Campbell et al. [8]. The interaction between the incident X-rays and Ge is now dominated by the L-shell electrons [29]. The escape of Ge L-shell photoelectrons produces a distribution starting around 1.2 keV which is similar to those of Mo and Rb, but more prominent. As we see from Table 5.3, escape fractions, P_{pe} = I(pe)/I(FEP), are generally higher than Monte Carlo predictions. Simulations underestimate escape of photoelectrons by a factor of two for Ag K X-rays, but it worsens as incident energy increases. This observation is by no means new. For example, in one of the earliest attempts [19] the low-energy tailing of the Ti K X-ray spectrum was observed to be ten times higher than that of Monte Carlo prediction. Similar discrepancies have also been reported by He et. al. [20]. More recently Campbell et al. [8] have commented that the ratio of the shelf intensity, at L-shell binding energy of Ge, to the main peak (i.e. FEP) is in close agreement for 2-and 3-keV photons, but at 7 keV this ratio approaches 1.5 in favor of the experiment. Finally, a study by Lowe [10], despite its success in estimating the spectral contribution of primary and secondary electrons, underestimated the overall intensity for L-sell photoelectron escape from a Ge detector at 5.9 keV.

To summarize, an analytical or Monte Carlo model which would give not only the correct positions but also the shapes, heights and intensities of the shelves for both Si and Ge detectors and for a wide range of incident energies seems to be an optimistic expectation. The effect of pulse shaping is perhaps a major factor influencing the spectral features of particularly the photoelectron escape. Since our Monte Carlo calculations were based purely on geometrical considerations, our results should be taken as a lower limit for the escape of photoelectrons.

In conclusion, we made a comprehensive study of partial energy loss mechanisms for a detector as a function of energy, and analyzed each mechanism both qualitatively and quantitatively. In light of the wide range of energies considered and the interactions studied, the overall agreement between our study and the published works cited here is quite reasonable.

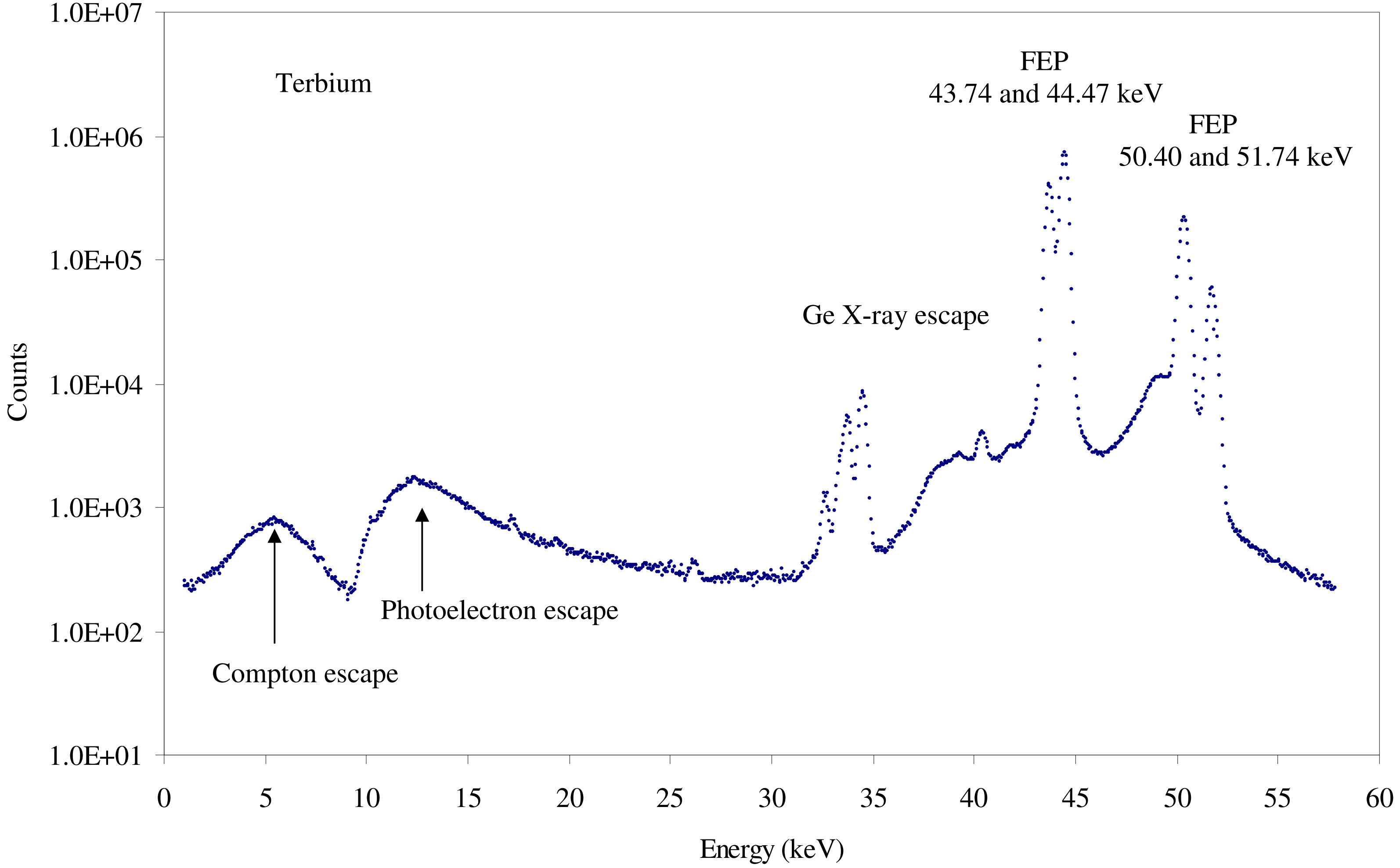

Figure 5.1: Spectrum of Tb.

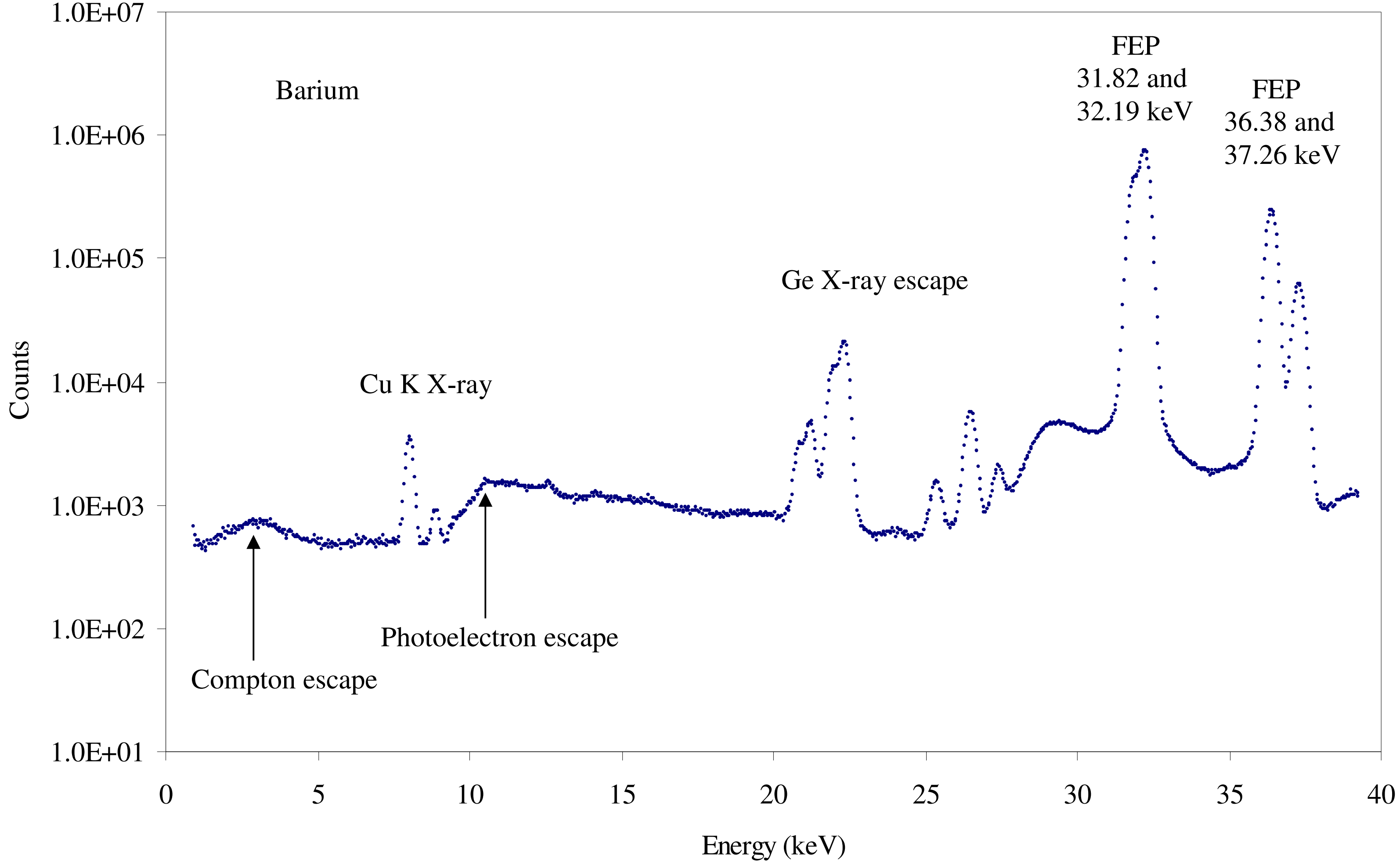

Figure 5.2: Spectrum of Ba.

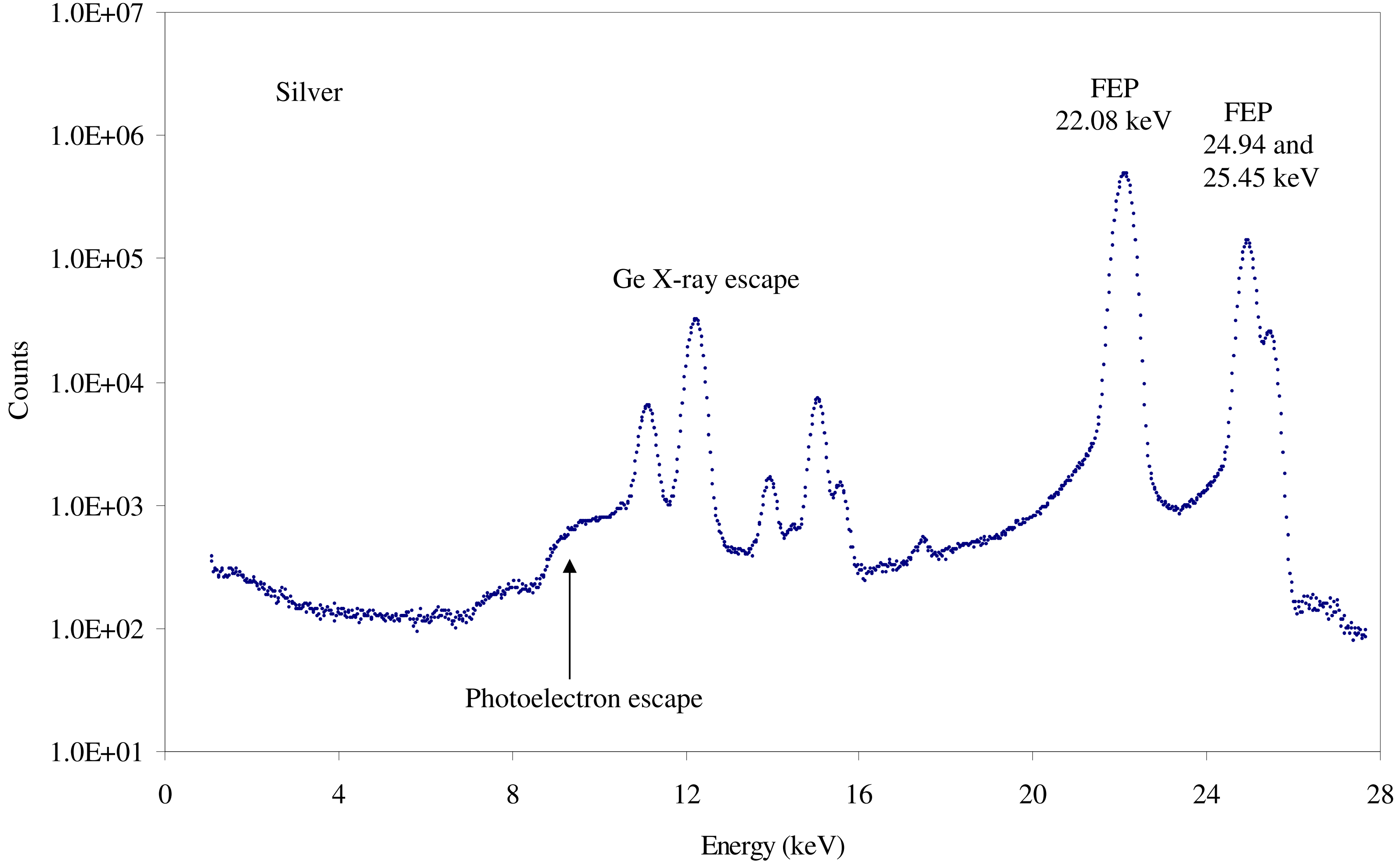

Figure 5.3: Spectrum of Ag.

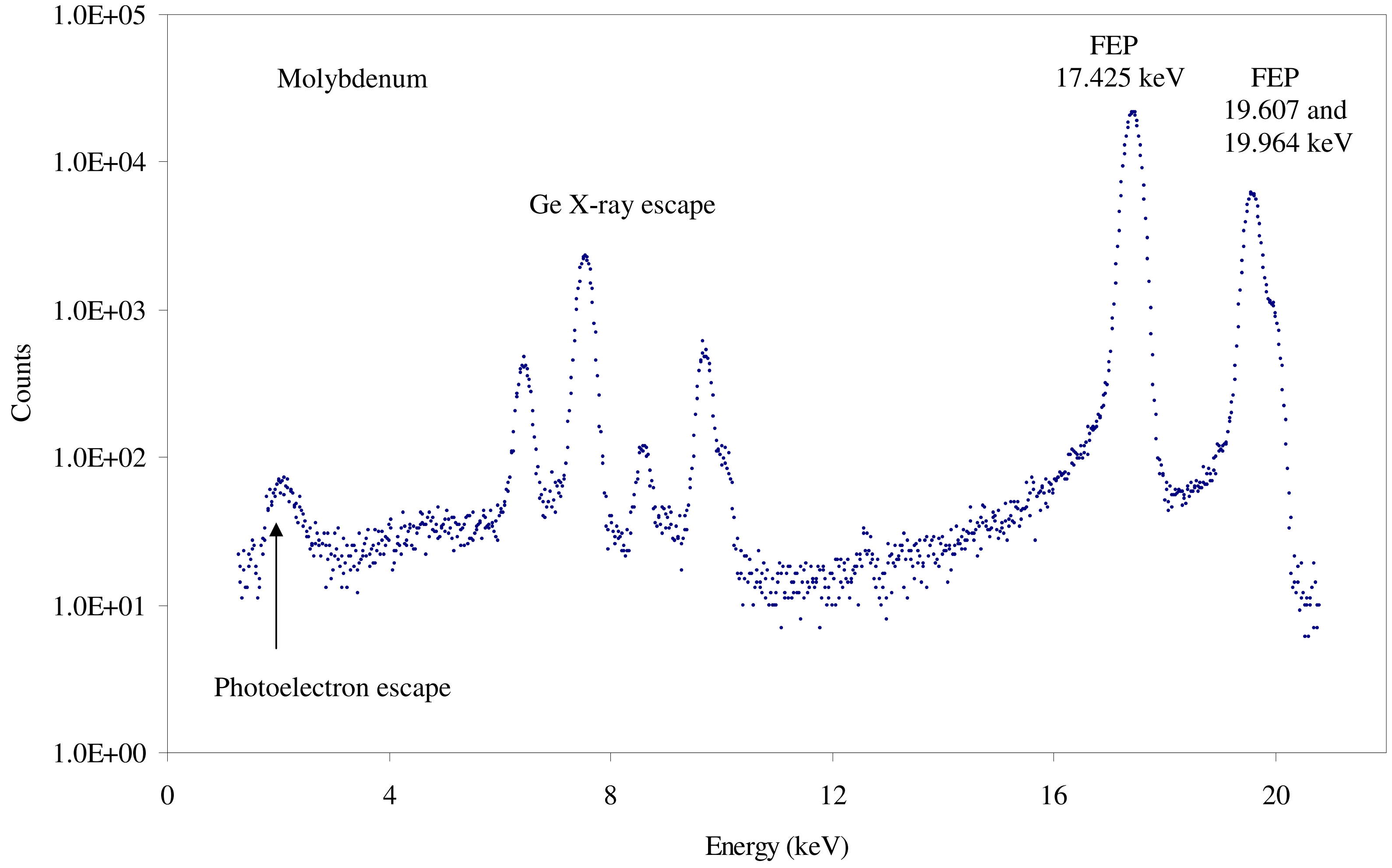

Figure 5.4: Spectrum of Mo.

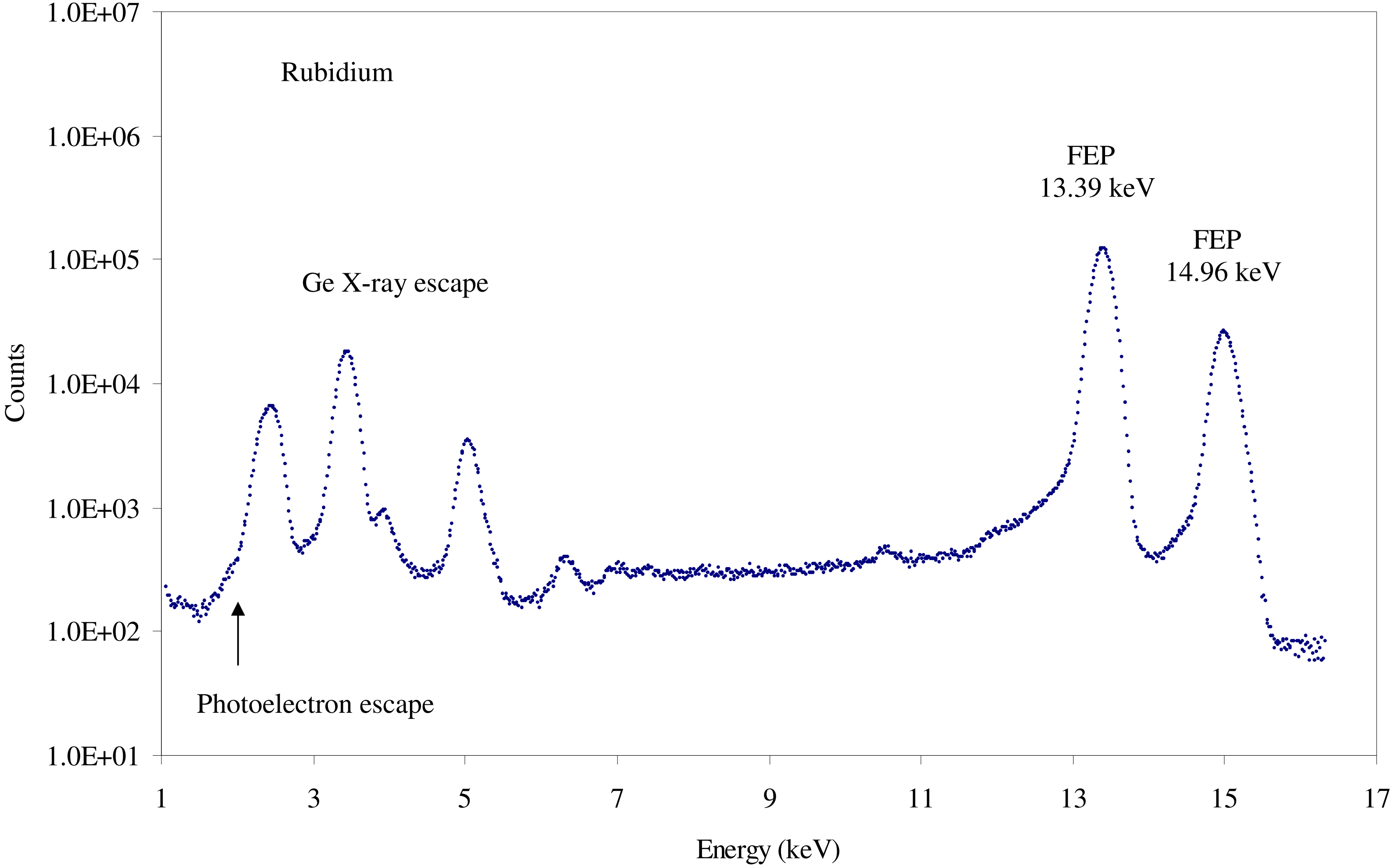

Figure 5.5: Spectrum of Rb.

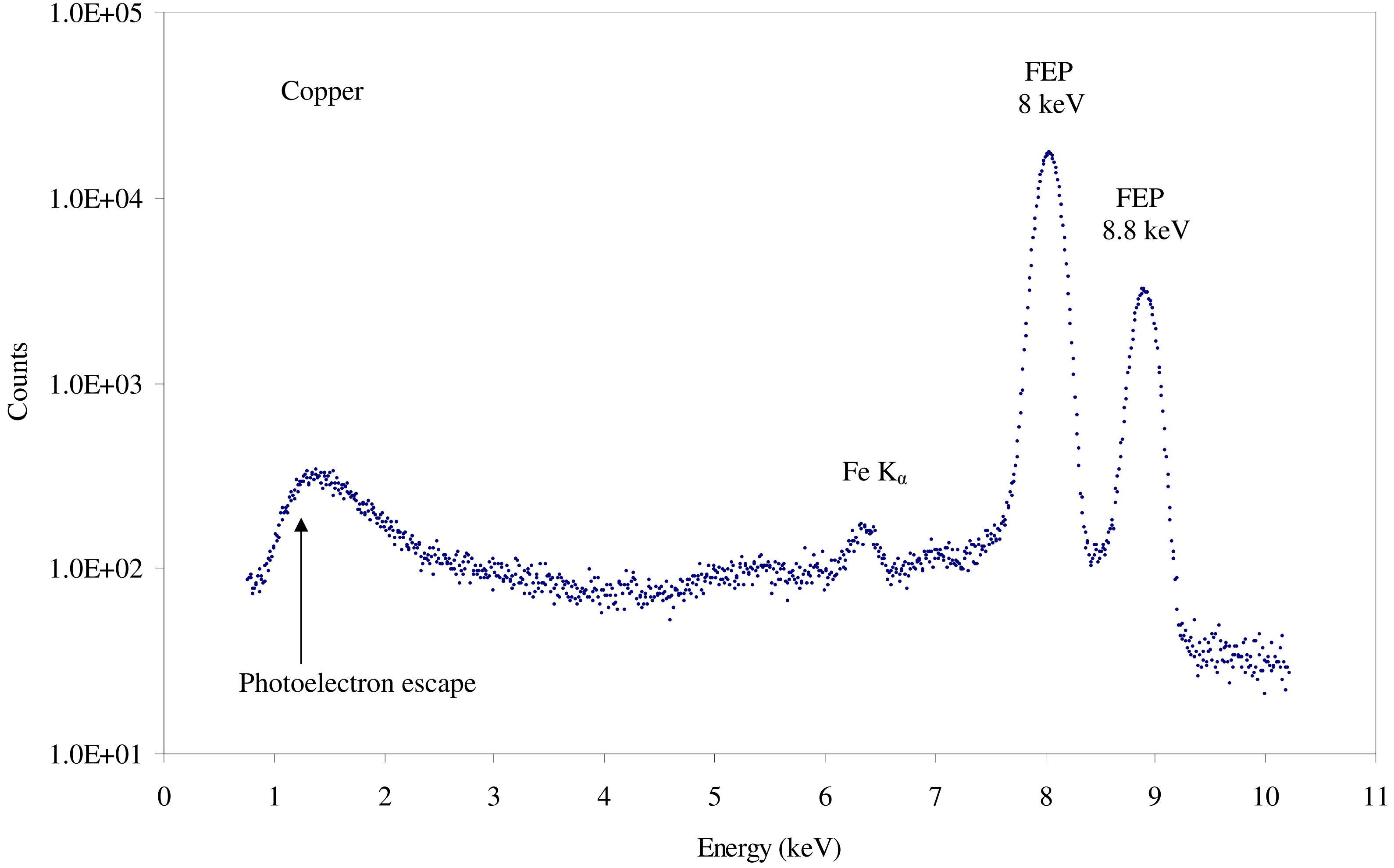

Figure 5.6: Spectrum of Cu.

Table 5.1: Ge X-ray escape fractions (in %).

		Our Experiment		Our Monte Carlo		Chan [15] MC.		Durak [17] Exp.	Christensen [12]				Seltzer [14] MC	
X-ray line	E (keV)	$P_{X\alpha}$	$P_{X\beta}$	$P_{X\alpha}$	$P_{X\beta}$	$P_{X\alpha}$	$P_{X\beta}$	$P_{X\alpha}$	$P_{X\alpha}$ Calc.	$P_{X\alpha}$ Exp.	$P_{X\beta}$ Calc.	$P_{X\beta}$ Exp.	$P_{X\alpha}$	$P_{X\beta}$
Rb K_α	13.37	13.0±0.05	1.8±0.02	12.5	1.9	12.2	1.7		13.6	13.0	2.0	2.1	11.9	1.8
Rb K_β	15.02	11.2±0.1	1.8±0.04	12.5	1.9	10.8	1.5						10.5	1.8
Mo K_α	17.44	9.2±0.1	1.6±0.04	10.8	1.6	9.0	1.3	10.9	9.4	9.0	1.5		8.8	1.5
Mo K_β	19.73	7.6±0.2	1.6±0.08	7.6	1.2	7.2	1.1	10.5					7.1	1.2
Ag K_α	22.10	6.2±0.02	1.2±0.01	6.6	1.1	6.2	1.0	6.5	6.2	6.1	1.1	1.1	6.0	1.1
Ag K_β	25.11	4.5±0.03	0.8±0.01	5.0	0.8	4.9	0.8	6.7					4.8	0.8
Ba K_α	32.06	2.6±0.01	0.5±0.004	2.6	0.5	2.8	0.5	2.6					2.7	0.5
Ba K_β	36.67	2.2±0.02	0.4±0.007	2.0	0.34	2.0	0.3	2.6					1.9	0.4
Tb K_α	44.22	1.1±0.01	0.2±0.003	1.2	0.2	1.2	0.2						1.2	0.2
Tb K_β	50.84			0.8	0.15	0.8	0.13						0.8	0.15
γ-ray [16]														
^{241}Am	59.54	0.53±0.01	0.08±0.003	0.48	0.09	0.51	0.09						0.50	0.1

Table 5.2: Compton and coherent escape fractions.

		P_{Com} (%)				P_{coh} (%)	
X-ray line	E (keV)	Our Exp.	Our MC	Chan [15]	Martin [2]	Our MC	Chan [15]
Rb K_α	13.37		0.02	0.02		0.05	0.06
Rb K_β	15.02		0.03	0.03		0.09	0.06
Mo K_α	17.44		0.05	0.05		0.10	0.06
Mo K_β	19.73		0.07	0.06	0.04	0.11	0.07
Ag K_α	22.10		0.09	0.06		0.10	0.09
Ag K_β	25.11		0.12	0.09		0.10	0.10
Ba K_α	32.06	0.12 ± 0.002	0.22	0.18	0.15	0.11	0.12
Ba K_β	36.67		0.31	0.21		0.12	0.09
Tb K_α	44.22	0.37 ± 0.004	0.50	0.41	0.35	0.11	0.08
Tb K_β	50.84		0.68	0.51		0.12	0.09
γ-ray [16]							
^{241}Am	59.54	0.70	0.91	0.80	0.80	0.11	0.10

Table 5.3: Photoelectron escape fractions.

P_{pe} (%)			
X-ray line	Experiment	Monte Carlo	Exp/MC
Ag	0.60 ± 0.004	0.32	2
Ba	1.60 ± 0.006	0.32	5
Tb	1.40 ± 0.007	0.28	5
γ-ray [16]			
^{241}Am	1.60 ± 0.01	0.22	7.4

REFERENCES

1. Papp T, Campbell JL. X-Ray Spectrom. 2001; **30**: 77.
2. Martin LJ, Burns PA. Nucl. Instrum. Methods A 1992; **312**: 146.
3. Pašić S, Ilakovac K. Nucl. Instrum. Methods A 1998; **405**: 45.
4. Can C. X-Ray Spectrom. (in press)
5. Campbell JL, Maxwell JA, Papp T, White G. X-Ray Spectrom. 1997; **26**: 223.
6. Tikkanen T, Kraft S, Scholze F, Thornagel R, Ulm G. Nucl. Instrum. Methods A 1997; **390**: 329.
7. Papp T, Campbell JL, Varga D, Kalinka G. Nucl. Instrum. Methods A 1998; **412**: 109.
8. Campbell JL, Cauchon G, Lepy M.-C, McDonald L, Plagnard J, Stemmler P, Teesdale WJ, White G. Nucl. Instrum. Methods A 1998; **418**: 394.
9. Lepy MC, Campbell JL, Laborie JM, Plagnord J, Stemmler P, Teesdale WJ. Nucl. Instrum. Methods A 2000; **439**: 239.
10. Lowe BG. Nucl. Instrum. Methods A 2000; **439**: 247.
11. Campbell JL, McDonald L, Hopman T, Papp T. X-Ray Spectrom. 2001; **30**: 230.
12. Christensen LH. X-Ray Spectrom. 1979; **8**: 146.
13. Fioratti MP, Piermattei SR. Nucl. Instrum. Methods 1971; **96**: 605.

14. Seltzer Stephen M. Nucl. Instrum. Methods A 1981; **188**: 133.

15. Chan H.-P, Chen C.-T, Doi K, Fewell TR, Shuping RE. Rad. Res. 1984; **99**: 443.

16. Can C. X-Ray Spectrom. (in press)

17. Durak R, Özdemir Y. Instrum. Science and Tech. 2001; **29**(3): 185.

18. Hight R, Inskeep CN. Adv. X-Ray Anal. 1978; **21**: 207.

19. Gardner RP, Yacout A.M, Zhang J, Verghese K. Nucl. Instrum. Methods A 1986; **272**: 399.

20. He HJ, Zhang TW, Shang RC, Xu SD. Nucl. Instrum. Methods A 1998; **272**: 847.

21. Joy DC. Rev. Sci. Instrum. 1985; **56**: 1772.

22. Geretschlager M. Nucl. Instrum. Methods B 1987; **28**: 289.

23. Goto S. Nucl. Instrum. Methods A 1993; **333**: 452.

24. Goto SJ. Synchrotron Radiat. 1998; **5**: 880.

25. Wang JX, Campbell JL. Nucl. Instrum. Methods B 1991; **54**: 499.

26. Aoki K, Koyama M. Phys. Med. Biol. 1990; **35**(8): 1051.

27. Hubbell JH. X-Ray Spectrum. 1999; **28**: 215.

28. http://physics.nist.gov/cgi-bin/Xcom/xcom3_1.

29. Storm E, Israel H. Nucl. Data Tab. A 1970; **7**: 565.

30. Hubbell JH, Trehan PN, Singh N, Chand B, Mehta D, Garg ML, Garg RR, Singh R, Puri S, J. Phys. Chem. Ref. Data 1994; **23**(2): 339.

31. Akheizer AI, Berestetskii VB Quantum Electrodynamics, Interscience Publishers, USA 1965: 429.

32. Knoll GF. *Radiation Detection and Measurement*, John Wiley and Sons, Inc., USA, 2001.

33. Berger MJ, http://physics.nist.gov/PhysRefData/Star/Text/ESTAR.html.

34. Klein O, Nishina Y. Z. Phys. 1929; **52**: 853.

35. Manninen SO, Cooper MJ, Cardwell DA, Nucl. Instrum. Methods A 1986; **245**: 485.

36. Ribberfors R, Berggren K-F. Phys. Rev. A 1982; **26**: 3325.

37. Biggs F, Mendelsohn LB, Mann JB. Atomic Data and Nucl. Data Tables 1975; **16**: 201.

38. Cromer DT. J. Chem Phys. 1969; **50**(11): 4857.

39. Hubbell JH, Veigele Wm. J, Briggs EA, Brown RT, Cromer DT, Howerton RJ. J. Phys. Chem. Ref. Data 1975; **4**(3): 471.

40. Jauch JM, Rohrlich F. *The Theory of Photons and Electrons*, Springer-Verlag, 1976.

41. Evans RD. *The Atomic Nucleus*, McGraw-HILL Book Company, 1969.

42. Cashwell ED, Everett CJ. *Monte Carlo Method*, Pergamon Press, 1959.

43. Veigele W. M. J. Atomic Data 1973; **5**: 75.

44. Mukoyama T, Nucl. Instrum. Methods 1976; **134:** 125.

APPENDIX A

The flowchart of the program

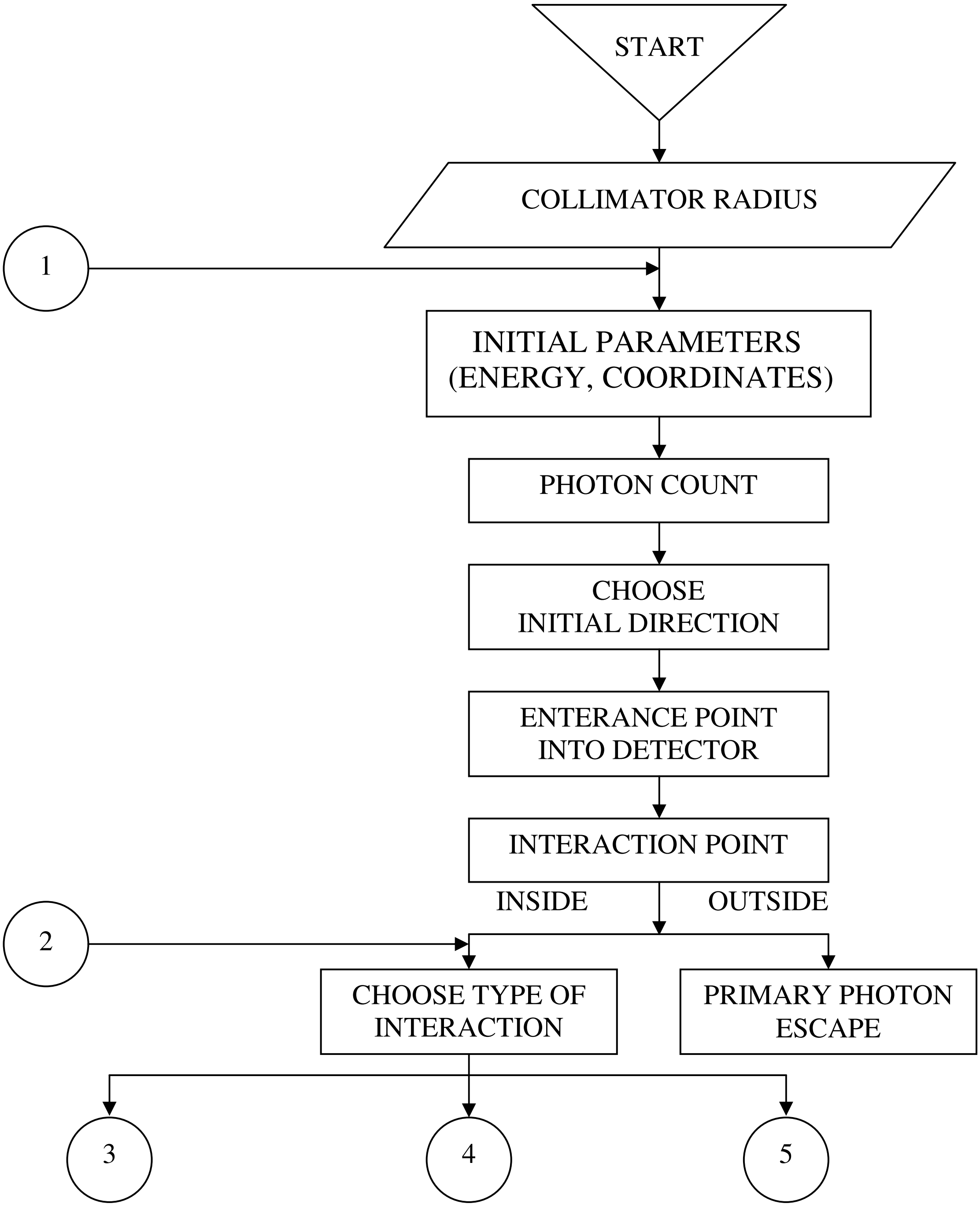

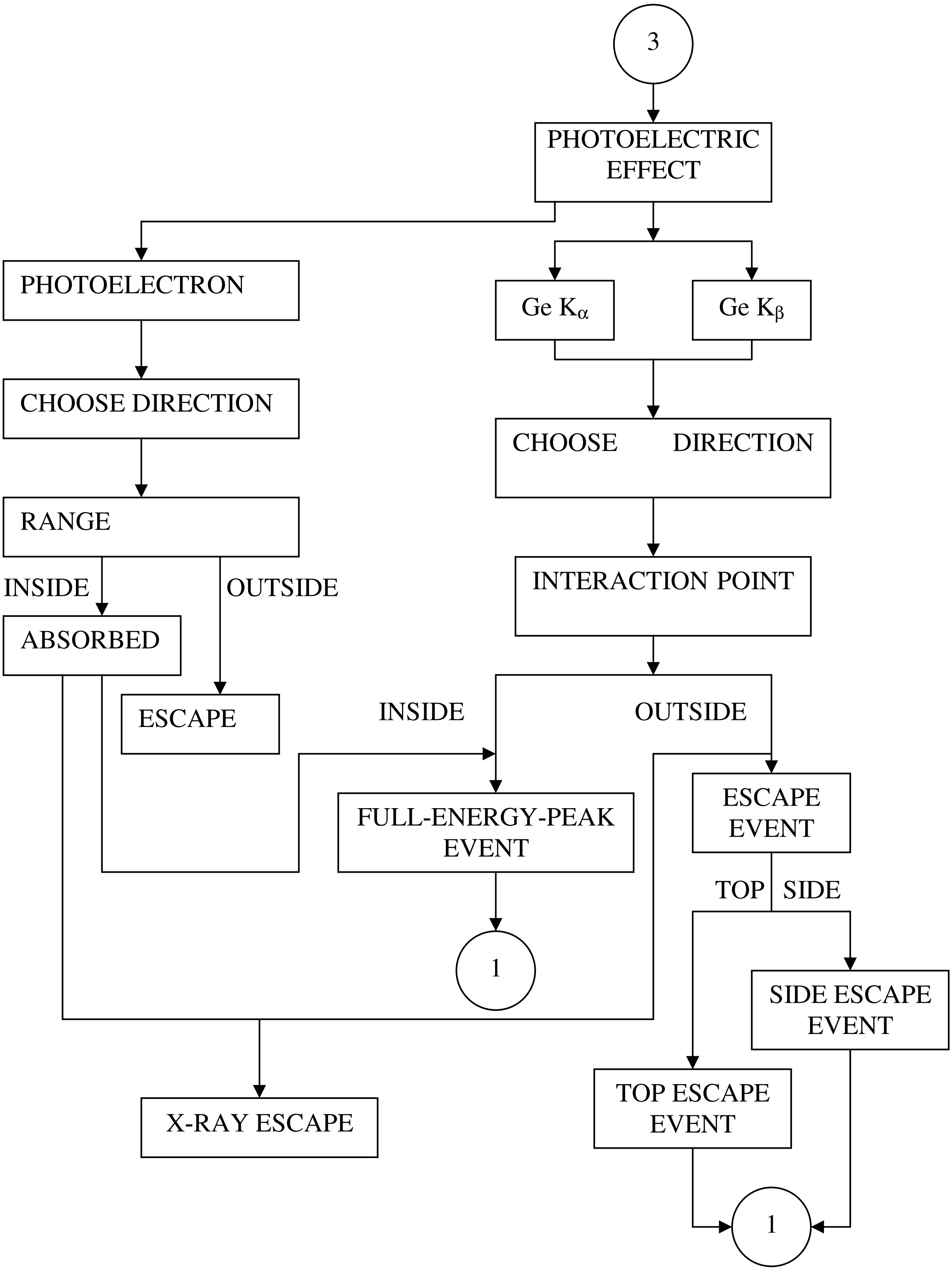
3
PHOTOELECTRIC EFFECT
PHOTOELECTRON
Ge Kα
Ge Kβ
CHOOSE DIRECTION
CHOOSE DIRECTION
RANGE
INSIDE
OUTSIDE
INTERACTION POINT
ABSORBED
ESCAPE
INSIDE
OUTSIDE
FULL-ENERGY-PEAK EVENT
ESCAPE EVENT
TOP
SIDE
1
SIDE ESCAPE EVENT
X-RAY ESCAPE
TOP ESCAPE EVENT
1

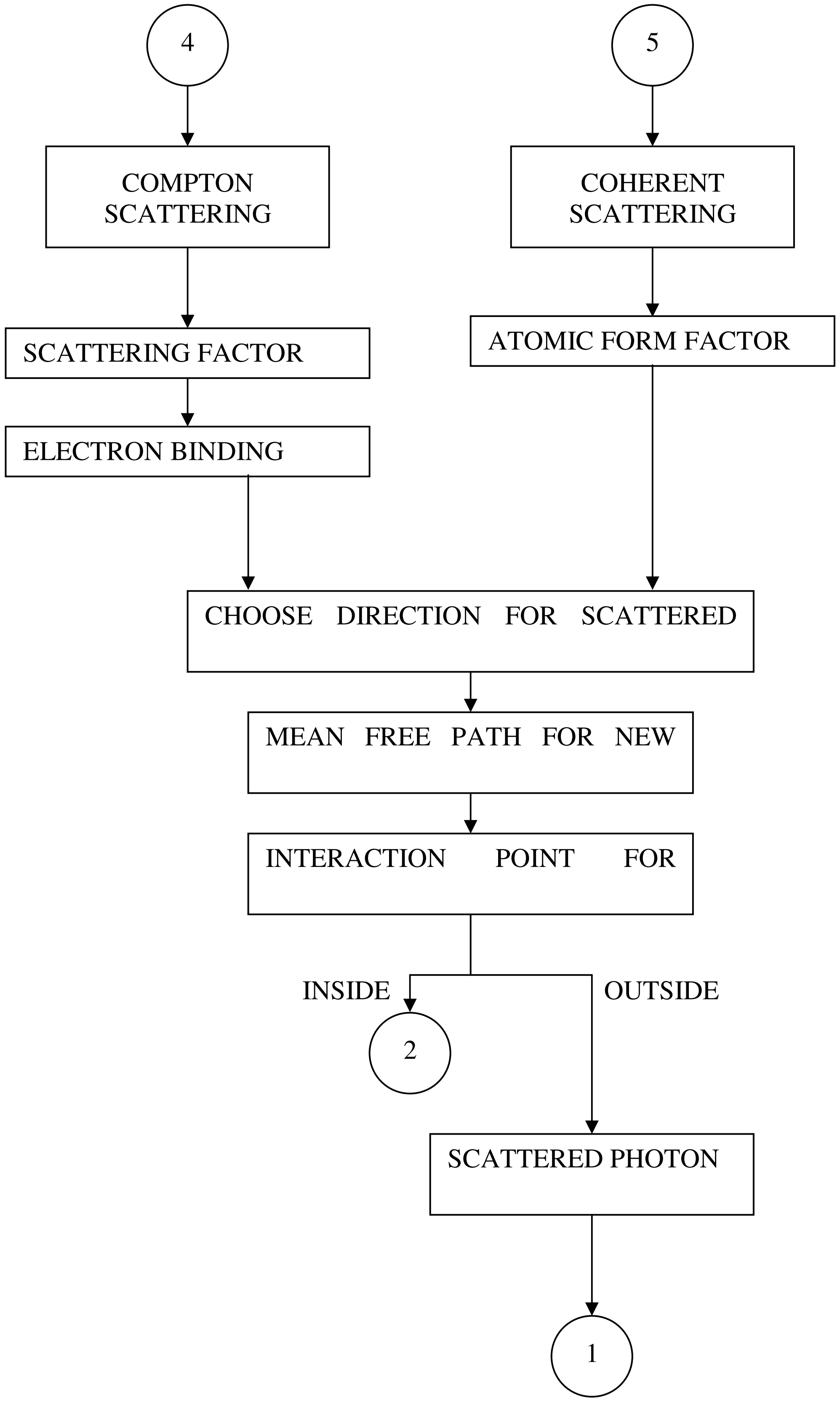
4
5
COMPTON SCATTERING
COHERENT SCATTERING
SCATTERING FACTOR
ATOMIC FORM FACTOR
ELECTRON BINDING
CHOOSE DIRECTION FOR SCATTERED
MEAN FREE PATH FOR NEW
INTERACTION POINT FOR
INSIDE
OUTSIDE
2
SCATTERED PHOTON
1

VITA

Ercan Yılmaz was born in Doğanşehir, Malatya on October 20, 1972. He received his B. S. degree in Physics department from the İnönü University in June 1995 and M. S. degree in Physics department from the Gazi University in May 1998. He worked in the Mustafa Kemal University as a Research Assistant from 1995 to 1999 in the department of Physics. He transferred to Middle East Technical University in August 1999. Since then he has been working as a research assistant in the Department of Physics at Middle East Technical University. His main areas of interest are Solar Energy and Atomic Physics.